Evolution in computed tomography: the battle for speed and dose

Lell, Michael M ; Wildberger, Joachim E ; Alkadhi, Hatem ; Damilakis, John ; Kachelriess, Marc

Abstract: The advent of computed tomography (CT) has revolutionized radiology. Starting as head-only scanners, modern CT systems are now capable of performing whole-body examinations within a couple of seconds in isotropic resolution. Technical advancements of scanner hardware and image reconstruction techniques are reviewed and discussed in their clinical context. These improvements have led to a steady increase of CT examinations in all age groups for a number of reasons. On the one hand, it is very easy today to obtain whole-body data for oncologic staging and follow-up or for trauma imaging. On the other hand, new examinations such as cardiac imaging, virtual colonoscopy, gout imaging, and whole-organ perfusion imaging have widened the application profile of CT. The increasing awareness of risks associated with radiation exposure triggered the development of a variety of dose reduction techniques. Effective dose values below 1 mSv, less than the annual natural background radiation (3.1 mSv/year on average in the United States), are now routinely possible for a number of dedicated examinations, even for coronary CT angiography.

DOI: https://doi.org/10.1097/RLI.0000000000000172

Evolution in Computed Tomography
The Battle for Speed and Dose

Michael M. Lell, MD, Joachim E. Wildberger, MD,† Hatem Alkadhi, MD,‡ John Damilakis, PhD,§ and Marc Kachelriess, PhD‖*

Abstract: The advent of computed tomography (CT) has revolutionized radiology. Starting as head-only scanners, modern CT systems are now capable of performing whole-body examinations within a couple of seconds in isotropic resolution. Technical advancements of scanner hardware and image reconstruction techniques are reviewed and discussed in their clinical context. These improvements have led to a steady increase of CT examinations in all age groups for a number of reasons. On the one hand, it is very easy today to obtain whole-body data for oncologic staging and follow-up or for trauma imaging. On the other hand, new examinations such as cardiac imaging, virtual colonoscopy, gout imaging, and whole-organ perfusion imaging have widened the application profile of CT. The increasing awareness of risks associated with radiation exposure triggered the development of a variety of dose reduction techniques. Effective dose values below 1 mSv, less than the annual natural background radiation (3.1 mSv/year on average in the United States), are now routinely possible for a number of dedicated examinations, even for coronary CT angiography.

Key Words: computed tomography, dose reduction, iterative reconstruction, dual-energy CT, metal artifact reduction, perfusion CT, dynamic contrast-enhanced CT, detector technology, CT angiography, low kV

(*Invest Radiol* 2015;00: 00–00)

Sir Godfrey Hounsfield, a British electrical engineer at EMI, and Alan MacLeod Cormack, a South African–born physicist were jointly awarded the Nobel Prize in Medicine in 1979 for their contributions to developing computed tomography, although they had worked independently from each other.[1] Johann Radon, an Austrian mathematician, had published much of the theoretical foundation of computed tomographic (CT) image reconstruction as early as 1917 (Radon transform).[2] In 1971, the first patient was imaged at Atkinson Morley's Hospital, London. The new insights into brain morphology possible with CT in patients received immediate worldwide scientific and media attention. This point in time is considered the beginning of a new era in clinical neuroscience. Early (first-generation) CT systems used a translate/rotate method, where the x-ray source, that only generated a pencil beam, and the detector moved laterally to cover the complete field of view, followed by a 1-degree rotation of the gantry. This process continued until 180 degrees were scanned. Such systems required 4 to 5 minutes to obtain the data for a single axial slice. Second-generation CT systems using a small x-ray fan beam were introduced in 1972; they still used the translate/rotate method. Both first- and second-generation systems were head-only scanners. Third-generation systems with a full x-ray fan beam that covered the complete field of view, and a simultaneously rotating tube and detector array were introduced in 1975. The geometry of modern CT systems is still similar to this setup. Fourth-generation systems with a full 360-degree detector ring and a rotating x-ray tube as well as electron beam CT were eventually both replaced by further developments of third-generation-type CT systems. In 1987, continuously rotating systems based on slip-ring technology were introduced with a gantry rotation time of 1 second. Spiral or helical CT was introduced in 1989[3] and led to a breakthrough in truly 3-dimensional (3D) CT imaging and in CT angiography (CTA). Cardiac CT was already announced in the 1970s[4,5] but was based on dedicated systems such as electron beam CT[6] and the dynamic spatial reconstructor.[7] It finally entered clinical routine and became widely available by combining the spiral trajectory on standard third-generation systems with a dedicated reconstruction approach.[8,9] In addition to the development of larger detector arrays with more detector rows, dual-source CT (DSCT) was introduced in 2005 with the aim of further increasing scan speed and double temporal resolution. High scan speed and temporal resolution had a strong impact on the technical development of CT and was particularly important for cardiac CT. The topic of cardiac CT is more completely covered in Wintersperger et al.[10]

SLICE WAR

In medical imaging, the *x*-*y* plane denominates the patient's cross section, whereas the *z*-direction denominates the longitudinal axis. A typical detector array consists of 800 to 1000 detector elements in-plane and of up to 320 detector rows in the *z*-direction. The general advantage of more rows is the simultaneous acquisition of more data along the patient's longitudinal axis, which mainly allows increased scan speed. In 1992, Elscint introduced the first third-generation CT system with two detector rows. With the availability of solid-state detectors based on scintillating ceramics,[11] the other CT vendors followed with 4-row detector arrays in 1998. Since then, a steady race for the highest number of active detector rows (or later slices per rotation) broke out, culminating in 2007 in 320 detector rows in the Toshiba Aquilion One (Table 1). The number of detector rows and slices acquired per rotation were equivalent until the introduction of 64-slice scanners. Whereas General Electric (GE), Philips, and Toshiba mounted 64-detector row panels, Siemens went a different way. Siemens implemented a double read-out technique called double *z*-sampling, which uses a periodic motion of the focal spot not only in the *x*-*y* (to double the number of rays per detector row) but also in the *z*-direction with the goal of doubling the number of independent slices acquired in the *z*-direction.[12,13] Philips later shared this concept when introducing their 256-slice system. Although the number of slices nominally doubles with this technique, the total width of the detector panel (and number of detector rows) does not change. Challenges associated with large detector panels are increased scatter, cone beam artifacts, heel effect, and a potential tradeoff in image quality.[14] On the other hand, broader detector panels cover more anatomy in a single rotation, optimally the whole organ of interest.

Received for publication February 20, 2015; and accepted for publication, after revision, April 8, 2015.

From the *Department of Radiology, University Hospital Erlangen, Erlangen, Germany; †Department of Radiology and Nuclear Medicine, Maastricht University Medical Center, Maastricht, the Netherlands; ‡Institute for Diagnostic and Interventional Radiology, University Hospital Zurich, Zurich, Switzerland; §Department of Medical Physics, University of Crete, Iraklion, Crete, Greece; and ‖X-Ray Imaging and CT, German Cancer Research Center (DKFZ), Heidelberg, Germany.

The authors report no conflicts of interest.

Correspondence to: Michael M. Lell, MD, Department of Radiology, University of Erlangen-Nuremberg, Ulmenweg 18, 91054 Erlangen, Germany. E-mail: michael.lell@uk-erlangen.de.

ISSN: 0020-9996/15/0000–0000
DOI: 10.1097/RLI.0000000000000172

TABLE 1. Data Sheet of Up-to-Date High-End CT Systems

CT System	Vendor	Configuration	Collimation (mm)	Cone (Degree)	Rotation (Second)	Max Power
Revolution CT	GE	256 × 0.625 mm Gemstone Clarity	160	15	0.28	103 kW Performix HDw
Brilliance ICT	Philips	2 · 128 × 0.625 mm NanoPanel^{3D}	80	7.7	0.27	120 kW iMRC
IQon	Philips	2 · 64 × 0.625 mm NanoPanel Prism	40	3.9	0.27	120 kW iMRC
Definition Edge	Siemens	2 · 64 × 0.6 mm Stellar	38.4	3.7	0.28	100 kW Straton
Definition Flash	Siemens	2 · 2 · 64 × 0.6 mm Stellar	38.4	3.7	0.28	2·100 kW Straton
Somatom Force	Siemens	2 · 2 · 96 × 0.6 mm Stellar^{Infinity}	57.6	5.5	0.25	2·120 kW Vectron
Aquilion ONE Vision	Toshiba	320 × 0.5 mm Quantum	160	15	0.275	100 kW MegaCool Vi

Names of detector and x-ray tube systems in Table 1 are trademarks. The notation of the detector configuration is the number of active detector rows × the slice thickness. An additional factor of 2 indicates that a *z* flying focal spot is used to double the number of slices. Another factor of 2 indicates that a dual-source dual-detector configuration is implemented. The collimation refers to the active width of the detector. All length values are scaled to the isocenter (*z*-axis).

Such detector panels facilitate interventional CT-guided procedures and expands the coverage in dynamic ("perfusion") CT.

GANTRY TECHNOLOGY

The introduction of slip-ring technology for the transport of data and energy to and from the gantry enabled continuous rotation of x-ray tube and detector. This was an essential prerequisite for the development of spiral CT scanners.[3,15] Most recent CT systems with gantry rotation times down to 0.25 s use noncontact data and energy transfer between the rotating and stationary parts of the gantry and some of them even friction-free air bearings. Tremendous centrifugal forces in the order of 40 g act on the rotating hardware, which weighs up to 1 ton and more. This has a significant impact on the x-ray tube design for mechanical reasons. Larger patient body sizes and the desire to perform whole-body scans also demand new patient table technology. To realize fast and particularly high-pitch scanning (table speeds of up to 74 cm/s are currently in use) the acceleration and deceleration range of the table needs to be taken into account to assure patient's comfort. The capacity of the CT table has been adapted to increasing patient's body weight, with special tables allowing 300 kg and more. Larger patients require not only increased table capacity but also greater gantry diameter (up to 90 cm in dedicated systems), extended reconstruction field of view, and higher tube output. In addition, a larger bore diameter provides more space for CT-guided interventions.

TUBE TECHNOLOGY

Despite the permanent struggle to reduce radiation exposure, increasingly powerful x-ray tubes have been developed to meet clinical needs. To perform a CT scan of chest and abdomen or an aortic CTA in heavy patients within a scan time short enough for the patients to comfortably hold their breath requires faster rotation times and table speeds, and therefore higher tube output is necessary. Typical maximum tube power is in the order of 100 kW or more. With dual-source systems, these values double. Since scan times significantly decreased during the past decades, the latest generation of x-ray tubes is optimized for very short exposure times at high exposure levels (Fig. 1A). Among vendors, a significant variation in maximum tube power performance can be observed (Fig. 1B).

Higher tube power does not mean higher patient's dose, but in contrast, it is potentially the basis of measures that significantly reduce the patient's dose. More x-ray power for instance allows using stronger prefiltration, which removes undesired low-energy photons from the spectrum, photons that would otherwise mainly contribute to the patient's dose but not to the CT image.

Higher output is also required if low-kilovolt scanning (see the "dose reduction techniques-low-kilovolt scanning" section below) is performed. Whereas the tube current can be selected freely in a relatively wide range, the tube voltage is typically limited to a few settings, although some recent systems allow operation at voltages ranging from 70 kV to 150 kV at 10 kV increments.[16–26] A flexible choice of tube voltages, including the possibility to go below 80 kV, is of importance for patient's dose reduction and contrast optimization and, in particular, for pediatric examinations.

In addition to allowing higher tube power values, x-ray tubes have also been optimized with the aim of minimizing cooling delays. This is possible by introducing direct (or active) cooling instead of using indirect cooling. One example of direct cooling is rotating envelope tubes where the anode is in contact with the envelope and where the envelope is in contact with a cooling medium: anode, cathode, and housing rotate together as a unit.[27] Another implementation of active cooling is to use spiral groove bearing technology, which replaces the conventional ball bearings and where liquid metal is used not only for lubrication (nonabrasive contact) but also to actively cool the anode.[28]

DETECTOR TECHNOLOGY

Since the late 1990s, CT detectors are indirect converters, where the x-ray energy is first converted into visible light, which then is captured by a photodiode and converted into an electric current (Fig. 2, left). Indirectly converting detectors in clinical CT systems are based on gadolinium oxysulfide (Gd_2O_2S, also called GOS or Gadox) ceramic scintillators. The scintillator material is optimized for high-dose usage, for high light output, for low crosstalk, and for low afterglow or ghosting. During the past years, detectors were further optimized with respect to electronic noise. This noise is intrinsic to the detector, showing up especially in the dark image (no x-ray exposure). Electronic noise is a noise source in addition to the x-ray quantum noise. Whereas quantum noise cannot be avoided, electronic noise can be reduced by decreasing the distance between the photodiode and the analog-to-digital converter electronics. This is achieved by designing more compact electronics that can be placed closer to the detector pixels and that require shorter analog wires. The latest step includes fully integrated electronics that have become possible with new contacting technology, the so-called through silicon vias.[29,30] With such a technology, the analog distance can be reduced to a few millimeters. Less electronic noise implies significantly lower image noise in those situations, where only few x-ray quanta reach the detector (obese patients, or very low milliampere second [mAs] settings as desirable for pediatric scans or screening programs).

Currently, semiconductor-based direct converting detectors are under development for CT imaging (Fig. 2, right).[31–33] With such a technology, a detected x-ray photon generates a very short pulse, short enough to count each photon. In addition, the area under the pulse, and thus the pulse height, is proportional to the photon energy. The aim is to design these photon-counting detectors with energy discrimination capabilities based on pulse height analysis to gather spectral x-ray information without the need to apply to different x-ray tube

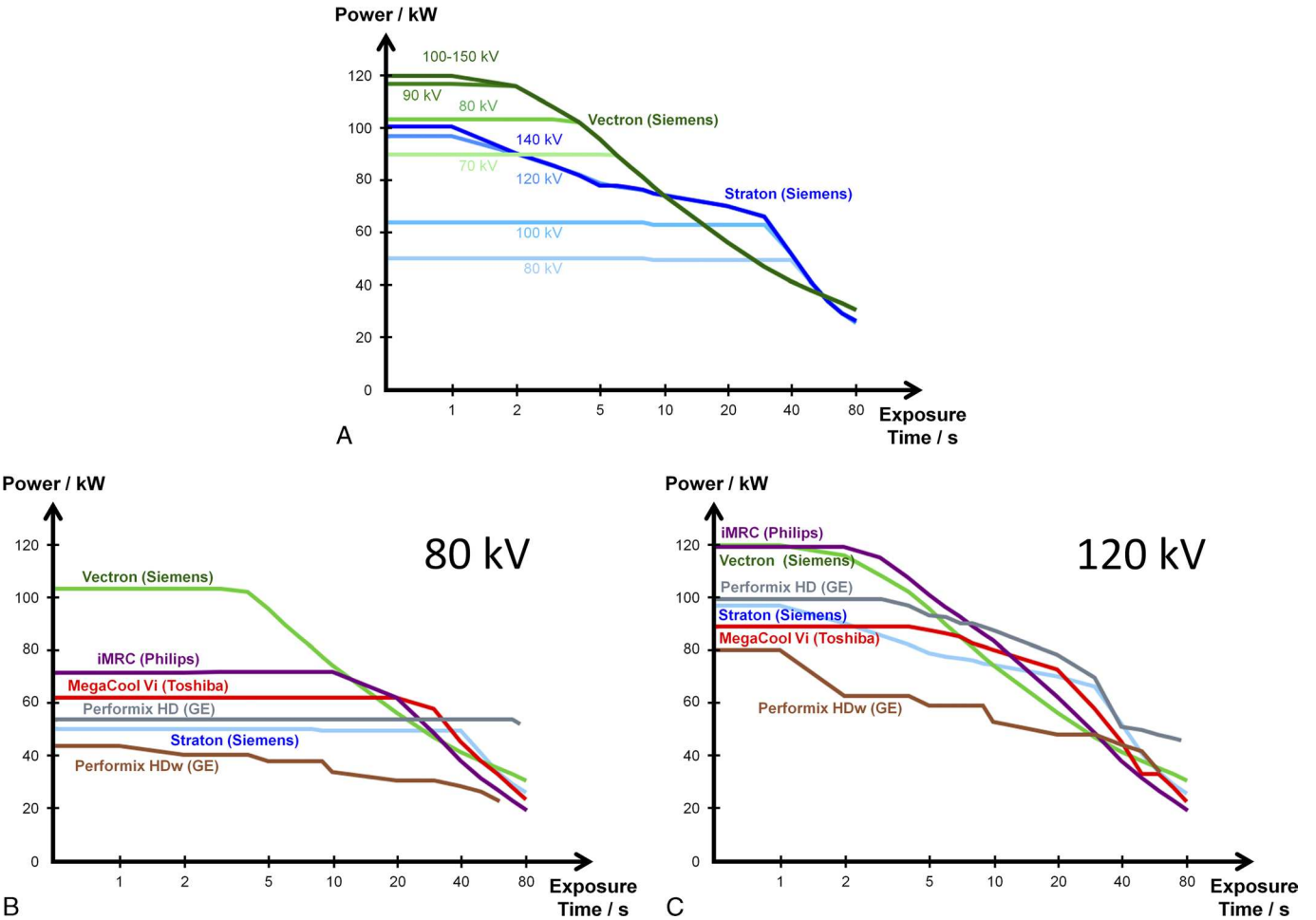

FIGURE 1. The available tube power is a function of the desired exposure time. The maximal tube power (eg, 120 kW) is available only for very short scans to avoid thermal damage to the anode. A, Two of the tubes are from the same vendor (blue, second last generation; green, latest generation). The trend to focus on shorter exposure times with high power levels is clearly visible. B, Tube performance across vendors at 80 kV. C, Tube performance across vendors at 120 kV. Plotted values are those available for routine spiral scanning at the scanner's console. Figure 1 can be viewed online in color at www.investigativeradiology.com.

voltages. These detectors are expected to improve tissue contrast and reduce image noise.[33] The latter is possible not only because the photon counters have zero electronic noise but also because the energy bin measurements can be combined in a statistically optimal way.[34] Dose reduction,[35] decreased beam hardening artifacts,[34] accurate K-edge imaging,[36,37] simultaneous multicontrast agent imaging,[38,39] and true quantitative imaging[40] are further potential benefits of this new detector generation. However, as of today, the technology is not yet mature, and only a few experimental systems exist that are not (yet) approved for patient examinations.

DOSE REDUCTION TECHNIQUES

Tube Current Modulation/Automatic Exposure Control

The technical basis for tube current adaption dates back to 1981.[41] Angular tube current modulation (TCM) resulted in 15% to 50% dose reduction, depending on the anatomical region in the x-y plane.[42] Online tube current modulation did not only reduce patient exposure but also homogenized noise distribution and therefore improved image quality.[43] The logical advancement of in-plane TCM was longitudinal or *z*-axis TCM. In analogy to angular modulation that considers different attenuation, in-plane (transverse projection vs anteroposterior projection at the level of the shoulders) longitudinal TCM aims to homogenize noise, taking into account the different attenuations, for example, of the chest as compared to the abdomen or pelvis. Different solutions from the major vendors became available using either a sinusoidal or attenuation-based online modulation algorithm. Automatic exposure control (AEC) consists of a group of algorithms, which incorporate (3D) TCM and aim to deliver a predefined image quality across a range of patient sizes derived from the topogram, increasing the volume CT dose index ($CTDI_{vol}$) for large and decreasing $CTDI_{vol}$ for small patients. Because AEC algorithms assume that the patient center is in the isocenter, correct centering is of importance. If the scan range goes beyond the range of the topogram, CT systems may act differently using either maximum or minimum mAs setting or something in between (standard mAs setting or mAs setting at the last calculated position). The image quality is defined differently for CT systems of different manufacturers: GE's AutomA uses a noise index that refers to the standard deviation of the CT value within a specific water phantom, which is converted to the individual patient; Philips' DoseRight uses a reference image, whereas Siemens' CareDose 4D uses reference mAs that defines the image quality in a "standard adult" of 70 kg body weight. Toshiba's ^{SURE}Exposure 3D offers at least three quality settings based on the target standard deviation of image noise. To allow comparison of protocols between different platforms,

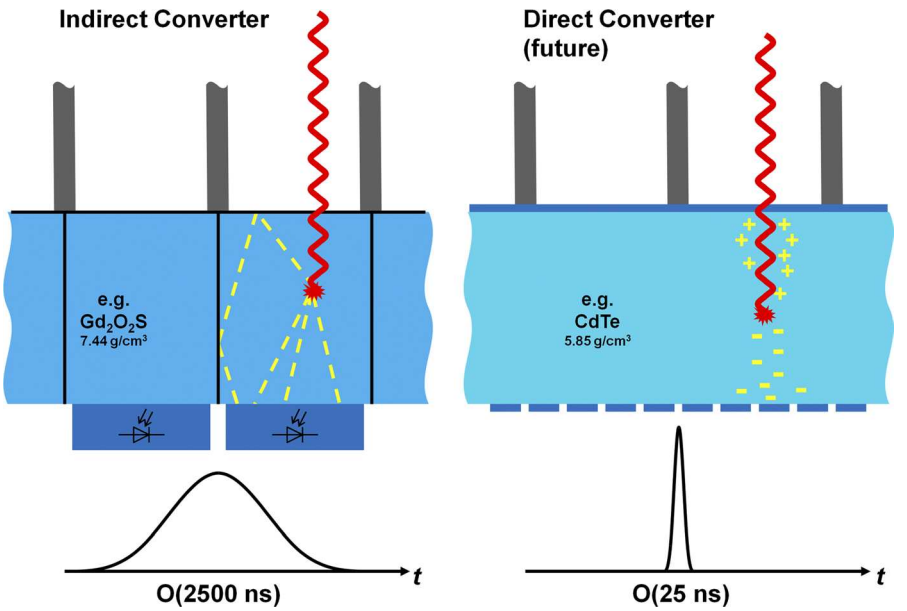

FIGURE 2. Conventional CT detectors (left) and future photon counters (right). Photon counting becomes possible owing to the very short signal peak generated by each x-ray photon, such that adjacently arriving photons typically generate two separate peaks. This is not the case for the indirect converters. Figure 2 can be viewed online in color at www.investigativeradiology.com.

not only the AEC setting or noise level but also the milliampere second and $CTDI_{vol}$ should be given.

Electrocardiogram (ECG)-correlated TCM reduces the tube output in phases of the cardiac cycle not intended for image reconstruction in retrospectively ECG-gated cardiac CTA. The shorter the time window with full tube output, the higher the dose reduction for the patient, at the cost of limited flexibility in image reconstruction of high-quality CTA data. Image reconstruction in those phases with very low x-ray exposure is still possible, which maintains the option to perform functional ventricular assessment.[44–48] A similar technique is available for prospectively gated scans, where the gating window can be chosen larger than necessary, and the full tube current will only be given to the minimum required range.

Dynamic Collimators

Detector panel width and pitch influence the *z*-overscanning effect, which is inherent to spiral CT. Spiral image reconstruction requires data from above and below each image position; therefore, at least one additional half-rotation (180 degrees in parallel ray geometry) is necessary at both ends of the spiral scan. As a result, additional tissue is exposed to radiation outside the imaged volume. For single–detector row scanners, *z*-overscanning may be considered irrelevant. However, the effect increases with the number of detector rows and becomes significant with large area detectors and cone-beam geometry. To minimize the *z*-overscanning effect, special dynamic collimators have been introduced that asymmetrically open and close at the edges of the scan range.[49]

Low-Kilovolt Scanning

Scanning at low-kilovolt setting increases the attenuation of contrast material (CM). For example, iodine attenuation increases by a factor of 1.97 (70 kV) and 1.44 (90 kV), respectively, compared with the one at 120 kV. Thus, the iodine dosage can be reduced by roughly 50% (70 kV) and 30% (90 kV) while maintaining identical attenuation.[19] The increased iodine attenuation can be used to reduce either the volume of CM,[50–52] or the radiation exposure (compensating higher image noise by higher contrast), or a combination of both. Operating the CT system at low-kilovolt at a fixed tube current minimizes the x-ray exposure of the patient but also increases image noise because fewer photons reach the detectors. In clinical practice, a change of the tube voltage setting requires a simultaneous adjustment of the tube current to keep image quality high. Therefore, low-kilovolt scanning, historically, was not popular in CT, except for perfusion CT, although the benefits in cardiac CTA,[21,53–57] aortic CTA,[58–60] and pediatric CT[23,61–63] have been demonstrated. Automatic selection of the tube voltage and adaption of the tube current, using information on the patient's attenuation from the localizer scan, and accounting for the planned examination type (nonenhanced scan, contrast-enhanced parenchymal scan, and CTA) translated this technology into routine use. Depending on the examination type, a dose reduction between 10% and 30% is possible.[16,17,25] The restricted x-ray tube output limited the automated selection of 80 kV or 100 kV in larger patients or with very fast scan modes. The recent availability of new high-performance x-ray tubes that provide very high tube currents at low tube voltages, however, makes low-kilovolt scanning routinely possible for a wide range of patients. Additional prefilters are in use for some protocols to remove undesired low-energy radiation from the low-kilovolt spectrum to maximize image quality and to minimize patient dose down to the level of conventional radiography.[18,22,26]

FAST SCANNING

The scan speed increases with an increased number of detector rows, although in some implementations, not all detector rows are available for spiral scanning. For dual-source CT systems, there is a special high-pitch mode, which is a very fast spiral scan mode that uses pitch values up to 3.2 to 3.4 and table speed of up to 737 mm/s. The data gaps occurring with single-source CT systems at pitch values greater than 1.5 are closed by the data from the second source in DSCT systems. Since the cone angle of DSCT is only half as large as the cone angle of single-source systems of twice the detector width, the same scan speed can be achieved with less cone beam artifacts (with the remaining cone beam artifacts being corrected by the iterative image reconstruction). The high pitch mode was originally designed to improve cardiac CTA.[53,56,64–76] All CT data of the heart are acquired in a

fraction of a single heartbeat (usually late diastole); thus, compared to a conventional low-pitch scan mode for cardiac CT with retrospective gating, no redundant data are acquired, which makes the scan mode very dose effective. In CT examinations that use all data for image reconstruction, the dose reduction effect vanishes, equal dose distribution within the scan range assumed.[61,66] Powerful tubes (Table 1) are necessary to deliver the required dose within that very short time, especially if low-kilovolt scanning is performed. Axial scanning with a large detector panel (up to 160 mm) covering the object of interest (eg, heart and brain) is an alternative[77–81] that does not require fast table speed with acceleration and deceleration but is limited in the length of *z*-coverage and faces some severe image quality challenges.[14]

Fast scanning offers a variety of advantages in daily practice; for example, the option to perform dose-effective ECG-triggered chest CTA ("triple-rule-out"),[58,82–85] to reduce the amount of CM in patients with renal impairment,[50,86–88] and to achieve a very homogeneous enhancement pattern. Scan times in the order of a second or less effectively help to suppress motion, for example, in patients who are not able to hold their breath or are unable to cooperate (small children, unconscious patients, severely impaired patients). In many cases, sedation is not necessary any more (Fig. 3).[20,58,61,89,90]

IMAGE RECONSTRUCTION

Filtered back projection (FBP) has been the reconstruction algorithm of choice during the recent decades. Filtered back projection is an analytical image reconstruction algorithm, that is, an inversion formula for a simplified measurement model. Filtered back projection is a reliable and robust algorithm that can be implemented with high computational performance. It has desirable properties such as linearity and translational invariance that make image quality easily understandable and facilitate image quality assessment (the image of the sum of two objects equals the sum of the object's individual images). However, owing to the simplicity of the measurement model, FBP cannot optimally account for a number of physical effects, such as the photon statistics, beam polychromaticity, or finite width x-ray beams. To account for the photon statistics empirical sinogram restoration approaches, so-called adaptive filters have been used for decades. With the introduction of multirow detector CT, the efficiency of such adaptive filtering improved tremendously owing to the possibility of filtering across detector rows or even across projections.[91] Adaptive filtering approaches are still in use today, and not just in combination with the FBP algorithm.

During the past decade, new classes of image reconstruction algorithms have become commercially available. Iterative image reconstruction approaches have been in use for a long time in nuclear medicine, but the lack of sufficient computing power prohibited their early implementation in CT (although Hounsfield's CT system was actually running an iterative reconstruction algorithm). Iterative reconstruction allows making use of more complicated measurement models than FBP and thereby promises images of lower artifact content and lower image noise. In contrast to FBP, this inversion is not based on finding a reconstruction formula but rather on iteratively estimating an image that best fits to the acquired raw data. This iterative estimation requires a series of iterations, however. Every iteration step consists of a forward projection, followed by a comparison of the forward-projected data with the measured raw data, followed by a back projection. This explains its high computational demands. Although a long list of publications focusing on iterative reconstruction techniques exists, insufficient data are published about the specific algorithmic implementation of the commercially available solutions.

The first iterative image reconstruction algorithms that became available commercially-adaptive statistical iterative reconstruction (ASIR; GE), adaptive iterative dose reduction (AIDR) and AIDR 3D (Toshiba), iterative reconstruction in image space (IRIS; Siemens), and iDose (Philips)-were purely image based (Fig. 3). These image postprocessing algorithms can be thought of being edge-preserving filtering, aiming at noise reduction in homogeneous regions and at preservation or improvement of spatial resolution at edges. In fact, the term *image restoration* would be more appropriate for these types of algorithms than the term *image reconstruction*.

In the meantime, vendors have provided "fully iterative image reconstruction algorithms" in the sense that the reconstructed image undergoes a forward projection to be compared with the measured raw data with the aim of minimizing the residual errors. This procedure is necessary to minimize artifacts such as cone beam or spiral artifacts. These raw data iterations can also be used to minimize image noise (for dose reduction) and to model the finite width and the exact shape of the x-rays (for resolution recovery). However, it can be shown that if an exact inverse of the forward projector exists, the iterative process can be converted into one that entirely operates in the image domain.[92] Furthermore, it can be shown that the effect of ray modeling in CT can also be converted to an image domain operation, given that this filtering is applied to a master image with rather small voxels.[93,94] These two observations justify minimizing the number of (computationally demanding) iterations between image domain and raw data domain in favor of performing more (computationally efficient) iterations in image domain (Fig. 4; Table 2).

Adaptive statistical iterative reconstruction (ASIR) is an iterative reconstruction algorithm of GE. Image noise is reduced by raw data preprocessing, FBP of the preprocessed raw data, modeling of the statistical system properties, and loop wise image regularization. The model incorporates statistical information from the CT system (including photon statistics and electronic noise) and details of the system optics (including the size of each detector cell, dimensions of the focal spot, shape, and size of each image voxel). The iterative procedure mainly involves the image data domain. The reconstruction time for this technique is only slightly longer than that for the FBP, therefore being well suited for the workflow of a busy imaging center. The

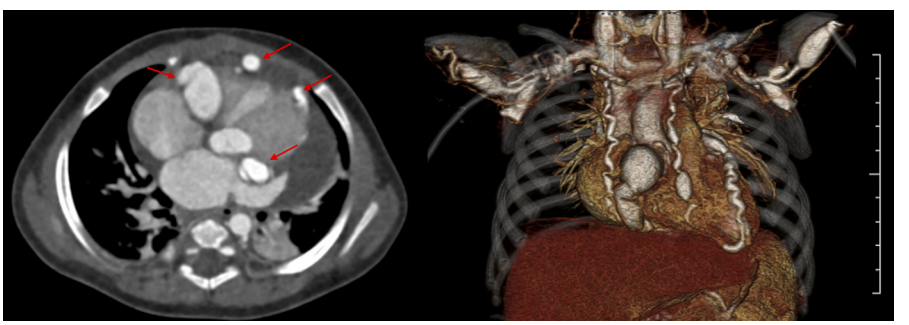

FIGURE 3. High-pitch pediatric CTA showing a 5-month-old boy with Kawasaki syndrome and multiple aneurysms; 70 kV; scan speed, 73 cm/s; pitch, 3.2; ADMIRE 2, $CTDI_{vol}$ (32 cm reference phantom), 0.27 mGy; dose length product, 4.5 mGy cm; effective dose, 0.47 mSv; no sedation required. Figure 3 can be viewed online in color at www.investigativeradiology.com.

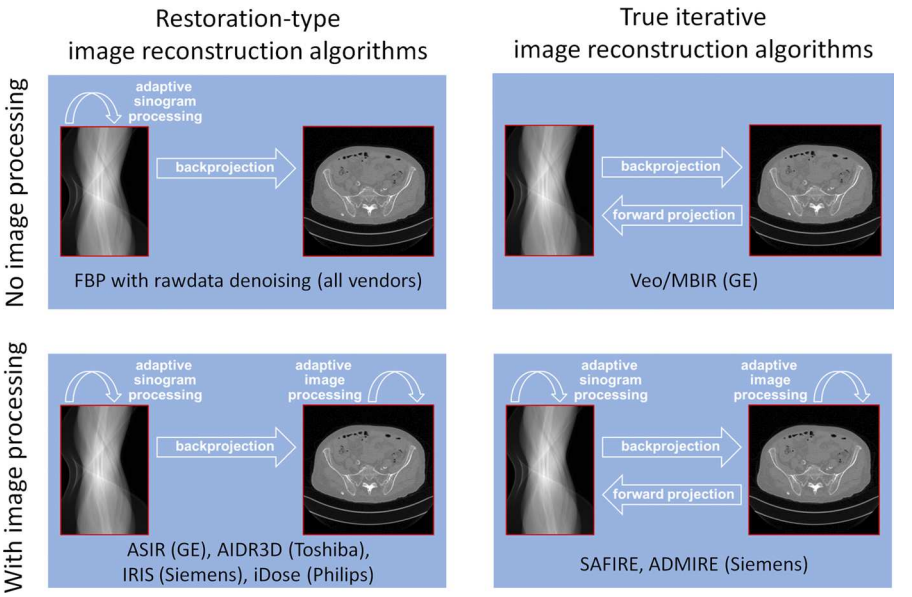

FIGURE 4. Classification of image reconstruction algorithms provided by the vendors (adapted from Kachelriess[95]). The algorithms are mostly a black box to the scientific community and users of the CT systems, with few details published. Two algorithms cannot be classified because the corresponding vendors do not disclose sufficient information (IMR [Philips], ASIR-V [GE]). Figure 4 can be viewed online in color at www.investigativeradiology.com.

regularization steps in the image domain affect not only the noise level but also the image texture, sometimes called "plastic-like" appearance. To improve acceptability and to restore the more familiar texture, ASIR images are typically linearly blended with FBP images. Zero percent ASIR corresponds to an FBP image, whereas 100% ASIR provides the highest level of noise reduction at the cost of an altered image texture. Increasing the blending ratio significantly decreases measured noise levels and increases signal-to-noise ratio (SNR) and contrast-to-noise ratio (CNR), but this does not necessarily translate into a significant improvement in diagnostic confidence and specificity.[96] In abdominal CT, weighting factors of 25% to 60% are frequently used.[96] With ASIR 40%, a dose reduction in abdominal CT of 25% has been realized.[97] In another study, body mass index (BMI) adapted dose reduction of 23% to 66% were reported, but the mean $CTDI_{vol}$ of the reference protocol in this study was very high (21 mGy for BMI < 20 kg/m^2 to 27 mGy for BMI > 25 kg/m^2).[98] Similar dose reduction potential was reported in cardiac CTA (44% dose reduction),[99] chest CT (25% dose reduction),[100] and head CT (31% dose reduction).[101]

Model-based iterative reconstruction (MBIR or VEO™, GE) is a computationally highly demanding "true" iterative reconstruction scheme; MBIR incorporates not only modeling of photon and noise statistics but also modeling of system optics.[26] Originally, blending with FBP images was not performed, and no specific reconstruction kernels were provided.[102–104] Dose reduction values of 50% and more without sacrificing image quality in abdominal CT were reported using MBIR.[105–108] When image qualities of abdominal CT were compared, MBIR images acquired at half (50%) standard-dose had less noise and better quality than half-dose ASIR and half-dose FBP, and also less noise and similar image quality compared with standard-dose FBP.[105] In another study of the abdomen and pelvis, subjective image quality of low-dose MBIR scans (76% dose reduction) was found to be superior compared to standard-dose FBP and ASIR.[107] In small liver lesions (<10 mm), detection and conspicuity were significantly higher with MBIR than with ASIR.[109] In low-dose chest CT, intraindividually comparing image quality of a 120 kV/50 mAs and 120 kV/4 mAs protocol, MBIR was criticized for blotchy pixelated appearance and reduced image sharpness compared to FBP. However, the performance of MBIR was significantly superior to that of FBP for the detection of noncalcified pulmonary nodules at the same dose level.[110] Submillisievert images ($CTDI_{vol}$, 2 mGy) were found to be diagnostically acceptable for the evaluation of lung parenchyma (not the mediastinum) even with FBP, but MBIR images at that dose were rated suboptimal because of

TABLE 2. Properties of the Iterative Reconstruction Techniques Used in CT Today

Vendor	Reconstruction Algorithm	Additional Parameters	Recon Time rel. to FBP	Sinogram Iterations	Image Iterations	Full Iterations
All	FBP	—	1	√	—	—
GE	ASIR, ASIR-V	0%–100% (eg, ASIR, 30%)	2	√	√	—
	MBIR/VEO	—	30–50	—	—	√
Philips	iDose	Levels 1–7	2	√	√	—
	IMR	Soft, Routine, or SharpPlus	5	?	?	?
Siemens	IRIS	Strength 1–5	1–2	√	√	—
	SAFIRE	Strength 1–5	1–2	√	√	√
	ADMIRE	Strength 1–5	1–2	√	√	√
Toshiba	AIDR, AIDR 3D	Mild, standard, or strong	1	√	√	—

The reconstruction time varies with different reconstruction hardware.

a loss of conspicuity of normal pulmonary structures despite showing the lowest image noise.[111] No significant differences in sensitivity between ASIR images ($CTDI_{vol}$, 1.77 mGy) and MBIR images ($CTDI_{vol}$, 0.39 mGy) were reported for ground glass opacities and nodules.[112] Filtered back projection, ASIR, and MBIR resulted in different emphysema indices and wall thickness measurements, which needs to be taken into account, when images from different sites and CT units are compared in the follow-up.[113] In head CT, MBIR was reported to be superior to ASIR in image quality and artifact reduction at equivalent dose level but at the cost of a mean reconstruction time of 32 minutes.[114] Higher resolution and lower noise have been reported at the cost of significantly longer reconstruction times (ranging from 10 to 90 minutes, depending on the number of slices to be reconstructed). Because the long reconstruction times significantly interfere with clinical workflow, a hybrid with ASIR (ASIR-V) is currently available instead of MBIR.

iDose 4 (Philips) is a hybrid iterative reconstruction algorithm with two denoising components: an iterative maximum likelihood-type sinogram restoration based on Poisson noise distribution and a local structure model fitting on image data that iteratively decreases the noise. The level of noise reduction in the images can be selected in 7 levels; the higher levels indicate greater noise reduction, also at the cost of increasing image texture alteration (blotchy pixilated appearance) compared to FBP images. Image reconstruction is fast enough not to delay the clinical workflow (approximately 20 frames per second).[115] Fifty-five percent dose reduction was reported using iDose in retrospectively ECG-gated coronary CTA using 256-multidetector computed tomography (MDCT).[116]

Iterative model reconstruction (IMR; Philips) is a more advanced algorithm, but very little detail has been published until now. The visibility of peripheral lung vessels on low-dose images ($CTDI_{vol}$, 1.8 mGy) reconstructed with iDose (levels 2 and 4) and standard-dose images ($CTDI_{vol}$, 5.6 mGy) reconstructed with FBP was considered optimal, but the visibility of small peripheral blood vessels on low-dose images reconstructed with IMR in a prototypic setting was compromised in some cases, although the overall noise level was lowest.[115] Intravascular noise reduction up to 88% in cardiac CTA was reported, with image noise amplitude within the left main coronary artery reduced by a factor of 1.3 from FBP to iDose 4 and by a factor of 2.6 from iDose 4 to IMR[117]; no correlation with invasive coronary angiography was performed, so the impact on stenosis grading could not be assessed.

Iterative reconstruction in image space (IRIS; Siemens) is an approach combining adaptive sinogram postprocessing, analytical image reconstruction, and iterative image processing. Similar to the other restoration type image reconstruction techniques, an initial FBP image containing all frequencies is used for subsequent iterative processing loops to enhance sharpness and reduce noise taking into account the physical properties of the scanner system and the reconstruction parameters. Repetitive correction loops account for noise reduction while preserving edge information and low-contrast structures.[118,119] The effect of IRIS could be elegantly assessed with DSCT, which allows acquisition of full-dose and half-dose CT data simultaneously by using data for image reconstruction from both or only one tube detector array. No statistically significant differences in diagnostic confidence or artifacts between full-dose FBP and 50% dose IRIS images of the abdomen were reported, except an altered image noise pattern with IRIS.[118] An identical setup was used to test the effects in chest CT with similar results.[120] Iterative reconstruction in image space significantly improved image quality compared to FBP images at the same dose level ($CTDI_{vol}$, 45 mGy) in head CT and at least matched the objective and subjective image quality parameters of standard FBP images ($CTDI_{vol}$, 60 mGy).[119]

Sinogram-affirmed iterative reconstruction (SAFIRE; Siemens) and the advanced modeled iterative reconstruction (ADMIRE; Siemens) are fully iterative. A few iterations between image and raw data domain are conducted to reduce artifacts. Noise reduction is conducted in sinogram and image domain. This combines high computational performance with high image quality.[92]

A similar DSCT approach as in reference[118] was used to assess image quality, diagnostic performance and the optimal strength setting of SAFIRE in abdominal CT. Sinogram-affirmed iterative reconstruction strength 2 (strength values ranging from 1 to 5 are available) at 50% dose was considered noninferior to FBP at full dose, although sensitivity for small lesions (<1 cm) was reduced using 50% SAFIRE (sensitivity, 55%) instead of 100% FBP (sensitivity, 70%; $P = 0.08$).[121] Acceptable image quality in cardiac CTA at very low dose (<0.1 mSv) became possible in selected patient groups using SAFIRE.[122] Chest CTA using low-kilovolt scan protocols and SAFIRE provided diagnostic image quality at low dose (<1.5 mSv).[123] Phantom (COPDGene 2 test object) measurements demonstrated accurate quantitative chest CT images with acceptable image noise at very low dose levels ($CTDI_{vol}$, 0.15 mGy) using ADMIRE.[124] Lower image noise, higher diagnostic confidence, and higher sensitivity for nodule detection was reported for ADMIRE compared to SAFIRE and FBP in low-dose chest CT (down to $CTDI_{vol}$, 0.14 mGy).[18]

The AIDR and AIDR 3D (Toshiba) are sinogram domain and image domain-based iterative reconstruction algorithms without a forward projection from image domain to sinogram domain.

METAL ARTIFACT REDUCTION

Artifacts from strongly attenuating objects like metallic implants, dental fillings, or highly concentrated contrast material (CM) are a problem frequently encountered in CT. They lead to severe image artifacts due to photon starvation, to beam hardening and, in particular, to scatter. Sometimes, such artifacts can be reduced using a physics-based approach.[125] In most cases, however, such severe artifacts require a dedicated metal artifact reduction (MAR) software.

The first algorithms for MAR, as well as many of the algorithms proposed since then are pure sinogram inpainting methods.[126,127] No matter how sophisticated the inpainting algorithm is, the original artifacts are removed, whereas significant new artifacts are introduced. The resulting images are rarely of diagnostic quality.

A decisive step toward diagnostic MAR images was the introduction of a so-called prior image, that is obtained from the initial uncorrected images by soft thresholding with the thresholds being set to represent the tissue classes air, soft tissue and bone, for example, with 3 predefined CT values. The normalized metal artifact reduction (NMAR) algorithm uses this prior image for normalization and denormalization. Forward projecting this prior image yields the prior sinogram, which is used to normalize the original raw data (Fig. 5). The normalized raw data are very homogeneous outside the metal trace; and thus, the metal trace can be safely replaced by linear interpolation or any other kind of inpainting approach. The inpainted raw data are then denormalized by pixelwise multiplication with the prior sinogram. The corrected raw data are reconstructed by FBP, the metal image is inserted, and, in some cases, high frequencies of the initial uncorrected images are added to obtain the final corrected images.[44,45] An iterative version of the NMAR algorithm, called IMAR is commercially being implemented on Siemens systems.[128] Another approach similar to the NMAR algorithm is the orthopedic metal artifact reduction (O-MAR) algorithm used commercially by Philips.[129] These new classes of MAR algorithms have been successfully used to improve image quality by suppressing metal artifacts in patients with dental[130–132] and orthopedic hardware.[133,134]

Virtual monochromatic imaging using dual-energy CT (DECT) (see the "Dual-Energy CT" section below) has been proposed as an alternative approach for MAR, but it has been demonstrated that DECT provides suboptimal image quality in patients with bilateral prostheses or in those with dental hardware.[135,136] Nevertheless, in cases where no dedicated MAR software is available, artifact reduction using such

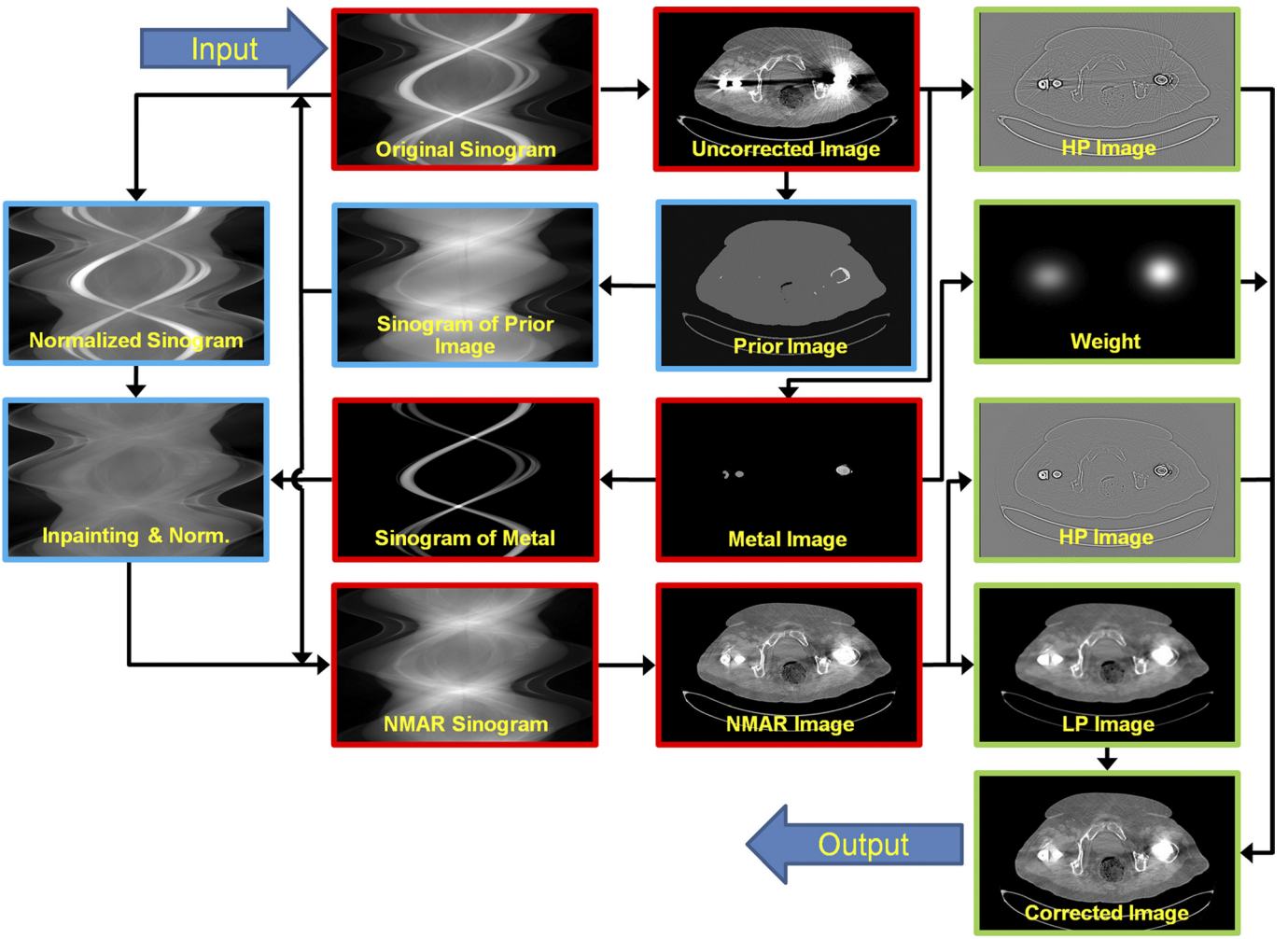

FIGURE 5. Dedicated metal artifact reduction algorithms either use simple inpainting (red), add prior information to normalize the data (red and blue), or additionally perform a frequency split to restore the noise texture (red, blue, and green). Figure 5 can be viewed online in color at www.investigativeradiology.com.

monochromatic DECT images may be a valuable alternative.[137,138] Flat-panel CT and cone-beam CT are considered alternative modalities in bone imaging, especially in the presence of metallic hardware, but MDCT has been demonstrated to provide sufficient image quality for postoperative imaging of internally fixated wrist fractures even without dedicated MAR algorithms.[139]

DUAL-ENERGY CT (DECT)

With the introduction of DSCT systems, DECT celebrated a revival from initial efforts of the 1980s.[140–143] Dual-energy CT makes use of the fact that attenuation can be decomposed into two linearly independent functions of energy, for example, into water and bone, into water and iodine, or, more physically, into photo and Compton effect. To allow for such decomposition, DECT performs a scan using two different x-ray spectra. Achieving optimal separation between the low- and the high-energy spectra is important in DECT because the quality of material decomposition depends on how different the two spectra are: the larger the difference between the two spectra, the smaller the noise level.

There are several implementations of DECT in routine clinical use (Fig. 6). Using two tubes, operating at different potentials, each tube's x-rays can be selectively prefiltered to minimize patient's dose and to improve spectral separation.[144] The additional prefilter on the high-energy x-ray source removes the undesired low-energy photons before they reach the patient. Another advantage of DSCT is that both x-ray tubes can be operated separately with individual tube currents and with individual tube current modulation curves (the low-energy thread requires larger modulation amplitudes than the high-energy thread).

Another implementation is based on fast tube voltage switching such that every other projection is performed at either the low- or the high-kilovolt value. This requires a dedicated x-ray tube and x-ray power generator, but selective prefiltering of the high-kilovolt x-rays is impossible. Owing to the finite rise and fall times of the tube voltage, the spectral separation is limited. In addition, the tube current cannot be switched owing to the temporal inertia of the filament and the required differences in mAs product for the low- and the high-kilovolt raw data can only partially be realized by setting the dwell times accordingly. An advantage of the kilovolt switching technology is that DECT can be provided in the full 50 cm field of measurement; and therefore, patient positioning is not as critical as with smaller field of measurements (26–35 cm), as it is the case with DSCT owing to space limitations.

Dual-layer, or sandwich, detectors are another alternative to realize full-field DECT. The first detector layer prefilters the x-rays; and thereby, the second layer sees the prefiltered x-rays that passed the first layer. Thus, the second layer measures the high-energy spectrum,

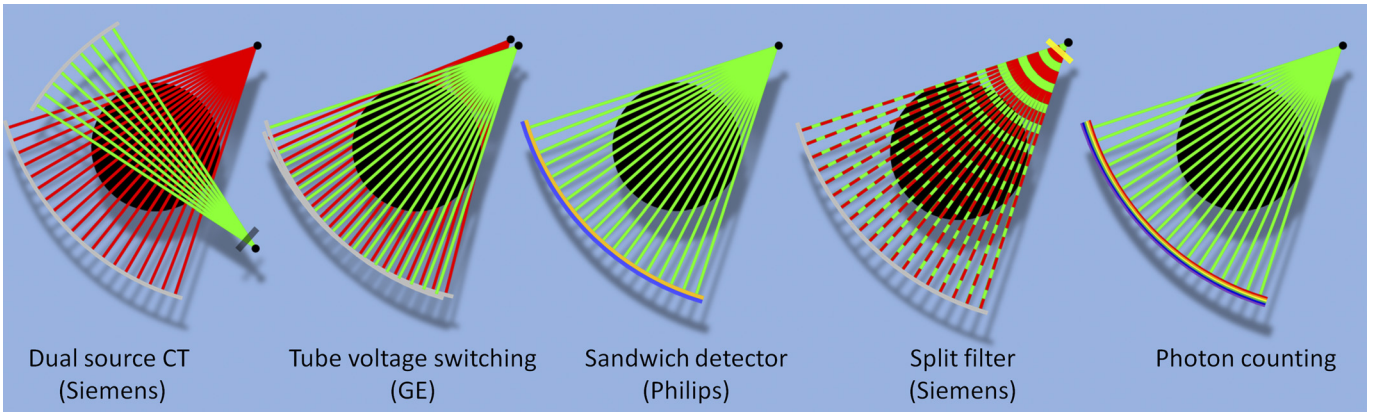

FIGURE 6. Today's dedicated DECT implementations and a potential future system with photon counting CT detectors. Not shown here is the option to do two subsequent scans with different tube voltages, as it is available for some mid-range CT systems. Figure 6 can be viewed online in color at www.investigativeradiology.com.

whereas the first layer mainly captures low-energy photons. The spectral separation cannot be adjusted with such systems, and separation will be limited, resulting in more noise. Sandwich detector DECT information provides geometrically fully consistent low- and high-energy data, which is not the case with the other implementations. Raw data-based DECT processing rather than image-based material decomposition is possible, and the user can retrospectively decide to use conventional single-energy CT or DECT information.

Recently, a split-filter technique was introduced in single-source CT, using a prefilter that is split along the *z*-direction such that (in the case of a 64-detector row system) the first 32 detector rows are prefiltered differently than the last 32 detector rows. A spiral pitch value below 0.5 needs to be chosen to ensure that each voxel is scanned with each of the two different spectra. The spectral separation achievable with such an approach is comparable to the sandwich detector and the tube voltage switching concepts. The system also provides spectral information throughout the full 50 cm field of measurement.

As previously mentioned, photon counting detectors are a highly promising technique for future diagnostic CT systems. Since these detectors can discriminate two or more energy windows, they are intrinsically suited for DECT applications. It should be noted that DSCT systems can potentially be equipped with one photon counting detector and one conventional energy integration detector, or with two photon counting detectors.

Typical clinical applications of DECT are virtual nonenhanced imaging,[145–147] automated bone removal,[148–151] urinary stone classification,[152–155] gout imaging,[80,156–162] metal artifact reduction,[135–138,163,164] cardiac[165–170] and pulmonary perfusion imaging,[171–183] and "monoenergetic" imaging (Figs. 7 and 8).[136,143,184–188] The very high CNR

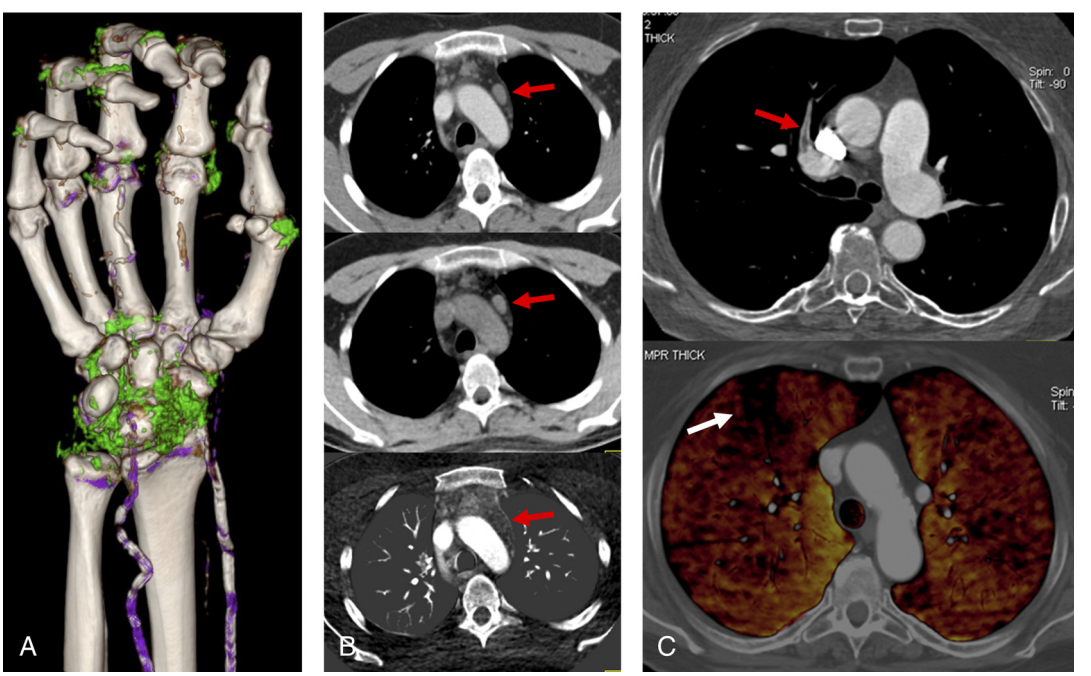

FIGURE 7. Typical examples of DECT. A, A 62-year-old patient with multiple urate deposits (coded in green color). Calcifications are coded in gray or purple (i.e, vessel walls). B, A 47-year-old patient after treatment of lymphoma. Persistent enlarged mediastinal lymph node (arrow) without contrast enhancement (upper row, 120-kV equivalent image; middle row, virtual nonenhanced image; bottom row, iodine map). C, A 68-year-old patient with acute pulmonary embolism. Embolic material (arrow) in CTA and the resulting perfusion defect (white arrow) in the color-coded iodine map (bottom row) can be visualized. Figure 7 can be viewed online in color at www.investigativeradiology.com.

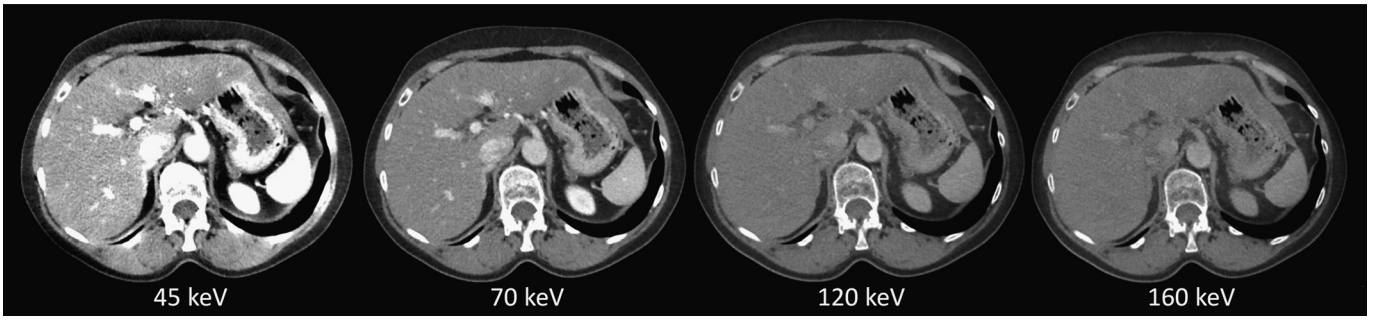

FIGURE 8. Energy dependence of iodine enhancement: monoenergetic imaging of a portal venous DECT realized with the split-filter technique. Very bright iodine contrast on 45-keV image (left) is gradually decreasing with increasing kiloelectron volt values.

in low–kiloelectron volt images can be used to either enhance the image contrast or to reduce the volume of CM while maintaining the CNR of a 120-kV image.

DYNAMIC CONTRAST-ENHANCED CT

Dynamic contrast-enhanced CT (DCE-CT) or perfusion CT (PCT) aims to assess the blood supply of tissue through analysis of the temporal enhancement pattern after CM injection. Rapid repetitive sampling of a specific tissue volume is performed while injecting a small volume of CM at a high injection speed.[189–191] The concentration of iodine within blood vessels and tissue is linearly proportional to the increase in attenuation; and therefore, the time-attenuation curve (TAC) can be analyzed for each voxel using a kinetic model. Hemodynamic parameters can be calculated from the distribution of CM in the intravascular and extracellular compartments: Mean transit time (MTT, time the tracer needs to travel through tissue vasculature), regional blood flow (BF, blood flow per tissue unit), blood volume (BV, fraction of blood per tissue unit), extraction fraction (E, fraction of tracer that is extracted to extracellular space during first pass), flow extraction product or permeability (FE or K_{trans}, tracer flow from intravascular into extracellular space per tissue unit), permeability surface area product (PS). Different techniques have been developed to postprocess the DCE data: for brain perfusion imaging, the deconvolution and maximum-slope approach; for tumor perfusion imaging, the deconvolution, Patlak method (BV, FE), and maximum slope. The limited volume coverage of older CT systems restricted the clinical use of DCE-CT predominantly to stroke imaging,[192–198] but the advent of high-frequency spiral techniques (variable pitch spiral) and very large area detectors[191,199–202] facilitated DCE-CT in whole-organ imaging. Lesion characterization, response prediction, and assessment are in the center of interest in oncologic imaging and extend the insights in tumor biology and treatment.[143,203–215] Dynamic contrast-enhanced CT is also used to assess physiological and pathophysiological organ function, for example, kidney function[190,199,212,216–225] or myocardial perfusion.[200,202,226–233] Myocardial perfusion imaging faces further challenges owing to the fast heart motion and the increased susceptibility to

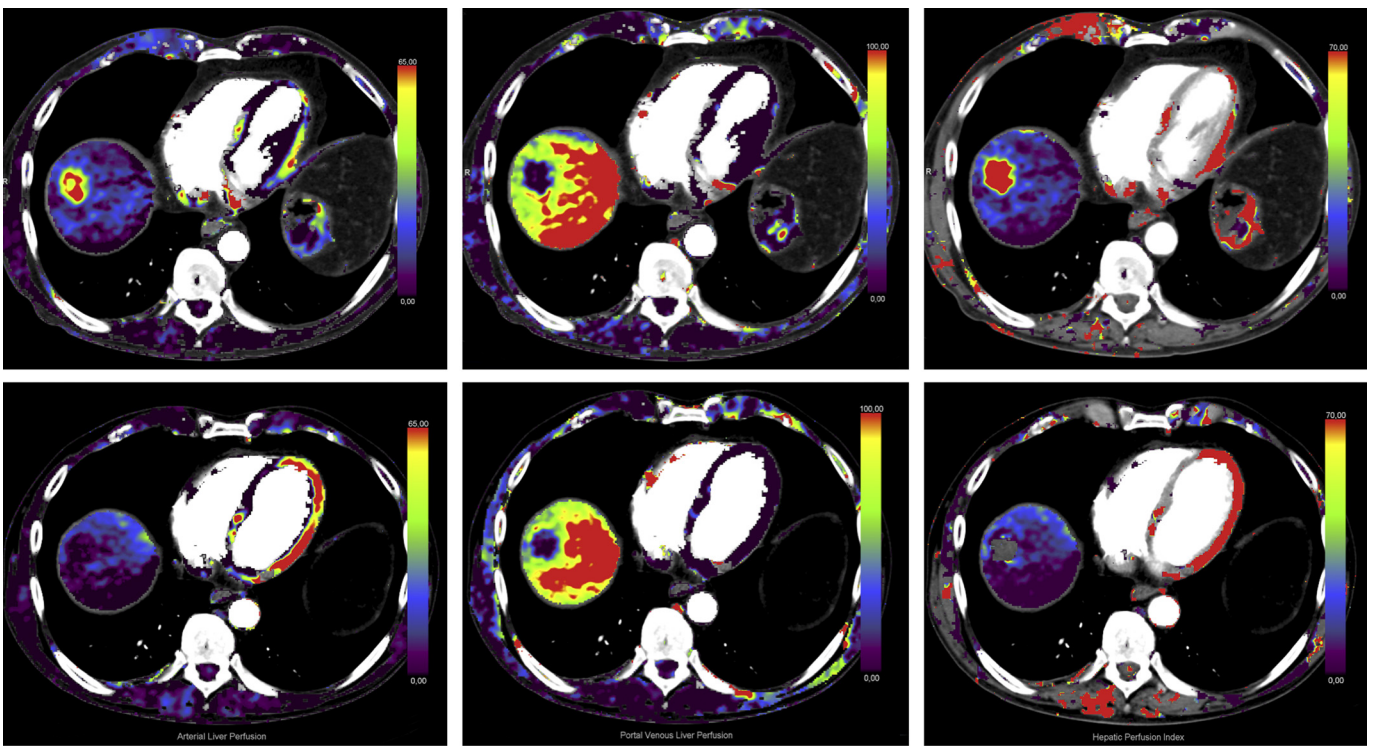

FIGURE 9. A 60-year-old man with HCC: upper row, before; bottom row, after therapy (TACE). Parameter maps demonstrate complete devascularization of the tumor after chemoembolization. From left to right, arterial liver perfusion, portal-venous liver perfusion, and hepatic perfusion index. Figure 9 can be viewed online in color at www.investigativeradiology.com.

artifacts. The heart motion can be compensated to some extent by synchronizing the acquisition with the ECG signal. However, this introduces strong limitations in the temporal resolution, which is often too low to follow the tracer dynamics, which are typically much faster in the heart than in other organs. For these reasons, further assumptions and efforts have to be made in the modeling step. Furthermore, beam hardening artifacts due to iodine or bone tend to change the CT values in the surrounding tissue.[234] Partial scan reconstruction used in cardiac CT to maximize the temporal resolution introduces CT value variations as a function of the start angle of the partial scan segment.[235] Dedicated algorithms to compensate for these inconsistencies need to be applied.[236–238] Chest perfusion imaging is discussed in more detail in Goo et al.[239]

Hepatic perfusion imaging[191,206,240–245] has gained special attention in a variety of clinical scenarios (tumor classification and grading, and therapy response assessment). Unlike most other organ systems, the liver (and lung) has a dual blood supply, necessitating adapted data postprocessing and modeling (Fig. 9).

Dynamic contrast-enhanced CT implies repetitive scanning of the same organ while the CM is passing the tissue of interest. Total scan times of 40 seconds up to several minutes have been proposed. This has two implications: patients are not able to hold their breath for such a long time, and radiation exposure increases. Registration and motion correction algorithms are used to cope with the first problem, low-kilovolt scanning, and all other means of dose reduction as previously described need to be considered for the second. Specific data such as the extracellular volume fraction and arterial enhancement fraction, which significantly correlate with hepatic fibrosis and cirrhosis, can also be determined with conventional multiphasic liver CT,[246,247] simplifying the process of data acquisition at moderate radiation exposure. As indicated in the previous section, DECT can provide iodine maps, which are often regarded as perfusion images, but it is important to recognize that DECT images do not reflect dynamic information but rather the iodine distribution inside an organ or a lesion at a specific time point.

CONCLUSIONS

Although repeatedly declared dead, CT has celebrated an amazing comeback within the past decade. Computed tomography is the workhorse in daily practice, spreading into new applications like cardiac and quantitative imaging, and shifting indications from radiography to CT with major clinical impact. Progress is seen with increased spatial resolution, faster scan speed, lower CM and radiation dose, and morphological and functional information. In 2014, approximately 81.2 million CT procedures were performed in the United States,[248] which on the one hand highlights the role of CT but on the other hand emphasizes the need for an intelligent dose management.

ACKNOWLEDGMENT

The authors thank Nico Buls, PhD, Thorsten Heußer, Ernst Klotz, PhD, Stefan Kuchenbecker, Francesco Pisana, Patrik Rogalla, MD, Rainer Schmitt, MD, and Martin Willemink, MD for their support.

REFERENCES

1. Hounsfield GN. Computed medical imaging. *Science*. 1980;210:22–28.
2. Radon J. Über die Bestimmung von Funktionen durch ihre Integralwerte längs gewisser Mannigfaltigkeiten. Berichte über die Verhandlungen der Königlich Sächsischen Gesellschaft der Wissenschaften zu Leipzig. *Mathematisch-Physische Klasse*. 1917;69:262–277.
3. Kalender WA, Seissler W, Klotz E, et al. Spiral volumetric CT with single-breath-hold technique, continuous transport, and continuous scanner rotation. *Radiology*. 1990;176:181–183.
4. Hounsfield GN. Nobel lecture, December 8, 1979. Computed medical imaging. *J Radiol*. 1980;61:459–468.
5. Sagel SS, Weiss ES, Gillard RG, et al. Gated computed tomography of the human heart. *Invest Radiol*. 1977;12:563–566.
6. Boyd DP, Lipton MJ. Cardiac computed tomography. *Proc IEEE*. 1983;71:298–307.
7. Robb RA, Ritman EL, Gilbert BK, et al. The DSR: a high-speed three-dimensional x-ray computed tomography system for dynamic spatial reconstruction of the heart and circulation. *IEEE Trans Nucl Sci*. 1979;NS-26:2713–2717.
8. Kachelriess M, Kalender WA. Electrocardiogram-correlated image reconstruction from subsecond spiral computed tomography scans of the heart. *Med Phys*. 1998;25:2417–2431.
9. Achenbach S, Ulzheimer S, Baum U, et al. Noninvasive coronary angiography by retrospectively ECG-gated multislice spiral CT. *Circulation*. 2000;102:2823–2828.
10. Wintersperger BJ, Bamberg F, De Cecco CN. Cardiovascular imaging: the past and the future, perspectives in computed tomography and magnetic resonance imaging. *Invest Radiol*. 2015;50:xxx–xxx.
11. Fuchs T, Kachelriess M, Kalender WA. Direct comparison of a xenon and a solid-state CT detector system: measurements under working conditions. *IEEE Trans Med Imaging*. 2000;19:941–948.
12. Kyriakou Y, Kachelriess M, Knaup M, et al. Impact of the z-flying focal spot on resolution and artifact behavior for a 64-slice spiral CT scanner. *Eur Radiol*. 2006;16:1206–1215.
13. Kachelriess M, Knaup M, Penßel C, et al. Flying focal spot (FFS) in cone-beam CT. *IEEE Trans Nucl Sci*. 2006;53:1238–1247.
14. Li B, Toth TL, Hsieh J, et al. Simulation and analysis of image quality impacts from single source, ultra-wide coverage CT scanner. *J Xray Sci Technol*. 2012;20:395–404.
15. Crawford CR, King KF. Computed tomography scanning with simultaneous patient translation. *Med Phys*. 1990;17:967–982.
16. Eller A, May MS, Scharf M, et al. Attenuation-based automatic kilovolt selection in abdominal computed tomography: effects on radiation exposure and image quality. *Invest Radiol*. 2012;47:559–565.
17. Eller A, Wuest W, Kramer M, et al. Carotid CTA: radiation exposure and image quality with the use of attenuation-based, automated kilovolt selection. *AJNR Am J Neuroradiol*. 2014;35:237–241.
18. Gordic S, Morsbach F, Schmidt B, et al. Ultralow-dose chest computed tomography for pulmonary nodule detection: first performance evaluation of single energy scanning with spectral shaping. *Invest Radiol*. 2014;49:465–473.
19. Lell MM, Jost G, Korporaal JG, et al. Optimizing contrast media injection protocols in state-of-the art computed tomographic angiography. *Invest Radiol*. 2015;50:161–167.
20. Lurz M, Lell MM, Wuest W, et al. Automated tube voltage selection in thoracoabdominal computed tomography at high pitch using a third-generation dual-source scanner: image quality and radiation dose performance. *Invest Radiol*. 2015;50:352–360.
21. Mahnken AH, Bruners P, Muhlenbruch G, et al. Low tube voltage improves computed tomography imaging of delayed myocardial contrast enhancement in an experimental acute myocardial infarction model. *Invest Radiol*. 2007;42:123–129.
22. Runge VM, Marquez H, Andreisek G, et al. Recent technological advances in computed tomography and the clinical impact therein. *Invest Radiol*. 2015;50:119–127.
23. Siegel MJ, Ramirez-Giraldo JC, Hildebolt C, et al. Automated low-kilovoltage selection in pediatric computed tomography angiography: phantom study evaluating effects on radiation dose and image quality. *Invest Radiol*. 2013;48:584–589.
24. Szucs-Farkas Z, Verdun FR, von Allmen G, et al. Effect of x-ray tube parameters, iodine concentration, and patient size on image quality in pulmonary computed tomography angiography: a chest-phantom-study. *Invest Radiol*. 2008;43:374–381.
25. Winklehner A, Goetti R, Baumueller S, et al. Automated attenuation-based tube potential selection for thoracoabdominal computed tomography angiography: improved dose effectiveness. *Invest Radiol*. 2011;46:767–773.
26. Lell MM, May MS, Brand M, et al. Imaging the parasinus region with a third-generation dual-source CT and the effect of tin filtration on image quality and radiation dose. *AJNR Am J Neuroradiol*. 2015. [Epub ahead of print].
27. Schardt P, Deuringer J, Freudenberger J, et al. New x-ray tube performance in computed tomography by introducing the rotating envelope tube technology. *Med Phys*. 2004;31:2699–2706.
28. Schmidt T, Behling M. MRC: a successful platform for future x-ray tube developments. *Medica Mundi*. 2000;44:50–55.
29. Duan X, Wang J, Leng S, et al. Electronic Noise in CT detectors: impact on image noise and artifacts. *AJR Am J Roentgenol*. 2013;201:W626–W632.
30. Shefer E, Altman A, Behling R, et al. State of the art of CT detectors and sources: a literature review. *Curr Radiol Rep*. 2013;1:76–91.
31. Kappler S, Henning A, Krauss B, et al. Multi-energy performance of a research prototype CT scanner with small—pixel counting detector. In: Nishikawa RM,

Whiting BR, Hoeschen C, eds. *Proceedings of SPIE: Medical Imaging 2013: Physics of Medical Imaging*. 2013;8668.

32. Schlomka JP, Roessl E, Dorscheid R, et al. Experimental feasibility of multi-energy photon-counting k-edge imaging in pre-clinical computed tomography. *Phys Med Biol*. 2008;53:4031–4047.
33. Taguchi K, Iwanczyk JS. Vision 20/20: single photon counting x-ray detectors in medical imaging. *Med Phys*. 2013;40:100901.
34. Schmidt TG. Optimal image-based weighting for energy—resolved CT. *Med Phys*. 2009;36:3018–3027.
35. Le HQ, Ducote JL, Molloi S. Radiation dose reduction using a CdZnT-based computed tomography system: comparison to flat-panel detectors. *Med Phys*. 2010;37:1225–1236.
36. Roessl E, Proksa R. K-edge imaging in x-ray computed tomography using multi-bin photon counting detectors. *Phys Med Biol*. 2007;52:4679–4696.
37. Shikhaliev PM. Photon counting spectral CT: improved material decomposition with k-edge-filtered x-rays. *Phys Med Biol*. 2012;57:1595–1615.
38. Anderson NG, Butler AP, Scott NJA, et al. Spectroscopic (multi-energy) CT distinguishes iodine and barium contrast material in mice. *Eur Radiol*. 2010;20: 2126–2134.
39. Clark DP, Badea CT. Spectral diffusion: an algorithm for robust material decomposition of spectral CT data. *Phys Med Biol*. 2014;59:6445–6466.
40. Ronaldson JP, Zainon R, Scott NJA, et al. Toward quantifying the composition of soft tissues by spectral CT with Medipix3. *Med Phys*. 2012;39:6847–6857.
41. Haaga JR, Miraldi F, MacIntyre W, et al. The effect of mAs variation upon computed tomography image quality as evaluated by in vivo and in vitro studies. *Radiology*. 1981;138:449–454.
42. Greess H, Wolf H, Baum U, et al. Dose reduction in computed tomography by attenuation-based on-line modulation of tube current: evaluation of six anatomical regions. *Eur Radiol*. 2000;10:391–394.
43. Kalender WA, Wolf H, Suess C. Dose reduction in CT by anatomically adapted tube current modulation. II. Phantom measurements. *Med Phys*. 1999;26: 2248–2253.
44. Jakobs TF, Becker CR, Ohnesorge B, et al. Multislice helical CT of the heart with retrospective ECG gating: reduction of radiation exposure by ECG-controlled tube current modulation. *Eur Radiol*. 2002;12:1081–1086.
45. Johnson TR, Nikolaou K, Busch S, et al. Diagnostic accuracy of dual-source computed tomography in the diagnosis of coronary artery disease. *Invest Radiol*. 2007;42:684–691.
46. Hermann F, Martinoff S, Meyer T, et al. Reduction of radiation dose estimates in cardiac 64-slice CT angiography in patients after coronary artery bypass graft surgery. *Invest Radiol*. 2008;43:253–260.
47. Mahnken AH, Bruners P, Schmidt B, et al. Left ventricular function can reliably be assessed from dual-source CT using ECG-gated tube current modulation. *Invest Radiol*. 2009;44:384–389.
48. Rutten A, Krul SP, Meijs MF, et al. Variability of coronary calcium scores throughout the cardiac cycle: implications for the appropriate use of electrocardiogram-dose modulation with retrospectively gated computed tomography. *Invest Radiol*. 2008;43:187–194.
49. Deak PD, Langner O, Lell M, et al. Effects of adaptive section collimation on patient radiation dose in multisection spiral CT. *Radiology*. 2009;252:140–147.
50. Meyer M, Haubenreisser H, Schoepf UJ, et al. Closing in on the K edge: coronary CT angiography at 100, 80, and 70 kV-initial comparison of a second-versus a third-generation dual-source CT system. *Radiology*. 2014;273:373–382.
51. Faggioni L, Neri E, Sbragia P, et al. 80-kV pulmonary CT angiography with 40 mL of iodinated contrast material in lean patients: comparison of vascular enhancement with iodixanol (320 mg I/mL)and iomeprol (400 mg I/mL). *AJR Am J Roentgenol*. 2012;199:1220–1225.
52. Szucs-Farkas Z, Schibler F, Cullmann J, et al. Diagnostic accuracy of pulmonary CT angiography at low tube voltage: intraindividual comparison of a normal-dose protocol at 120 kVp and a low-dose protocol at 80 kVp using reduced amount of contrast medium in a simulation study. *AJR Am J Roentgenol*. 2011;197:W852–W859.
53. Goetti R, Leschka S, Baumuller S, et al. Low dose high-pitch spiral acquisition 128-slice dual-source computed tomography for the evaluation of coronary artery bypass graft patency. *Invest Radiol*. 2010;45:324–330.
54. Thomas CK, Muhlenbruch G, Wildberger JE, et al. Coronary artery calcium scoring with multislice computed tomography: in vitro assessment of a low tube voltage protocol. *Invest Radiol*. 2006;41:668–673.
55. Gerber TC, Stratmann BP, Kuzo RS, et al. Effect of acquisition technique on radiation dose and image quality in multidetector row computed tomography coronary angiography with submillimeter collimation. *Invest Radiol*. 2005;40: 556–63.
56. Achenbach S, Marwan M, Ropers D, et al. Coronary computed tomography angiography with a consistent dose below 1 mSv using prospectively electrocardiogram-triggered high-pitch spiral acquisition. *Eur Heart J*. 2010;31:340–346.
57. Kim MJ, Park CH, Choi SJ, et al. Multidetector computed tomography chest examinations with low-kilovoltage protocols in adults: effect on image quality and radiation dose. *J Comput Assist Tomogr*. 2009;33:416–421.
58. Lell M, Hinkmann F, Anders K, et al. High-pitch electrocardiogram-triggered computed tomography of the chest: initial results. *Invest Radiol*. 2009;44:728–733.
59. Szucs-Farkas Z, Schaller C, Bensler S, et al. Detection of pulmonary emboli with CT angiography at reduced radiation exposure and contrast material volume: comparison of 80 kVp and 120 kVp protocols in a matched cohort. *Invest Radiol*. 2009;44:793–799.
60. Schindera ST, Graca P, Patak MA, et al. Thoracoabdominal-aortoiliac multidetector-row CT angiography at 80 and 100 kVp: assessment of image quality and radiation dose. *Invest Radiol*. 2009;44:650–655.
61. Lell MM, May M, Deak P, et al. High-pitch spiral computed tomography: effect on image quality and radiation dose in pediatric chest computed tomography. *Invest Radiol*. 2011;46:116–123.
62. Elgeti T, Proquitte H, Rogalla NE, et al. Evaluation of a reduced dose protocol for respiratory gated lung computed tomography in an animal model. *Invest Radiol*. 2007;42:230–234.
63. Papadakis AE, Perisinakis K, Raissaki M, et al. Effect of x-ray tube parameters and iodine concentration on image quality and radiation dose in cerebral pediatric and adult CT angiography: a phantom study. *Invest Radiol*. 2013;48:192–199.
64. Achenbach S, Marwan M, Schepis T, et al. High-pitch spiral acquisition: a new scan mode for coronary CT angiography. *J Cardiovasc Comput Tomogr*. 2009;3: 117–121.
65. Ertel D, Lell MM, Harig F, et al. Cardiac spiral dual-source CT with high pitch: a feasibility study. *Eur Radiol*. 2009;19:2357–2362.
66. Flohr TG, Leng S, Yu L, et al. Dual-source spiral CT with pitch up to 3.2 and 75 ms temporal resolution: image reconstruction and assessment of image quality. *Med Phys*. 2009;36:5641–5653.
67. Hausleiter J, Bischoff B, Hein F, et al. Feasibility of dual-source cardiac CT angiography with high-pitch scan protocols. *J Cardiovasc Comput Tomogr*. 2009;3:236–242.
68. Lell M, Marwan M, Schepis T, et al. Prospectively ECG-triggered high-pitch spiral acquisition for coronary CT angiography using dual source CT: technique and initial experience. *Eur Radiol*. 2009;19:2576–2583.
69. Leschka S, Stolzmann P, Desbiolles L, et al. Diagnostic accuracy of high-pitch dual-source CT for the assessment of coronary stenoses: first experience. *Eur Radiol*. 2009;19:2896–2903.
70. Alkadhi H, Stolzmann P, Desbiolles L, et al. Low-dose, 128-slice, dual-source CT coronary angiography: accuracy and radiation dose of the high-pitch and the step-and-shoot mode. *Heart*. 2010;96:933–938.
71. Kuefner MA, Hinkmann FM, Alibek S, et al. Reduction of X-ray induced DNA double-strand breaks in blood lymphocytes during coronary CT angiography using high-pitch spiral data acquisition with prospective ECG-triggering. *Invest Radiol*. 2010;45:182–187.
72. Neefjes LA, Dharampal AS, Rossi A, et al. Image quality and radiation exposure using different low-dose scan protocols in dual-source CT coronary angiography: randomized study. *Radiology*. 2011;261:779–786.
73. Scharf M, Bink R, May MS, et al. High-pitch thoracic CT with simultaneous assessment of coronary arteries: effect of heart rate and heart rate variability on image quality and diagnostic accuracy. *JACC Cardiovasc Imaging*. 2011;4: 602–609.
74. Sun K, Han RJ, Ma LJ, et al. Prospectively electrocardiogram-gated high-pitch spiral acquisition mode dual-source CT coronary angiography in patients with high heart rates: comparison with retrospective electrocardiogram-gated spiral acquisition mode. *Korean J Radiol*. 2012;13:684–693.
75. Neefjes LA, Rossi A, Genders TS, et al. Diagnostic accuracy of 128-slice dual-source CT coronary angiography: a randomized comparison of different acquisition protocols. *Eur Radiol*. 2013;23:614–622.
76. Hell MM, Bittner D, Schuhbaeck A, et al. Prospectively ECG-triggered high-pitch coronary angiography with third-generation dual-source CT at 70 kVp tube voltage: feasibility, image quality, radiation dose, and effect of iterative reconstruction. *J Cardiovasc Comput Tomogr*. 2014;8:418–425.
77. Barfett JJ, Fierstra J, Mikulis DJ, et al. Blood velocity calculated from volumetric dynamic computed tomography angiography. *Invest Radiol*. 2010;45:778–781.
78. Blobel J, Mews J, Schuijf JD, et al. Determining the radiation dose reduction potential for coronary calcium scanning with computed tomography: an anthropomorphic phantom study comparing filtered backprojection and the adaptive iterative dose reduction algorithm for image reconstruction. *Invest Radiol*. 2013;48:857–62.

79. de Graaf FR, Schuijf JD, van Velzen JE, et al. Diagnostic accuracy of 320-row multidetector computed tomography coronary angiography to noninvasively assess in-stent restenosis. *Invest Radiol*. 2010;45:331–340.
80. Diekhoff T, Kiefer T, Stroux A, et al. Detection and characterization of crystal suspensions using single-source dual-energy computed tomography: a phantom model of crystal arthropathies. *Invest Radiol*. 2015;50:255–260.
81. Neubauer J, Voigt JM, Lang H, et al. Comparing the image quality of a mobile flat-panel computed tomography and a multidetector computed tomography: a phantom study. *Invest Radiol*. 2014;49:491–497.
82. Halpern EJ. Triple-rule-out CT angiography for evaluation of acute chest pain and possible acute coronary syndrome. *Radiology*. 2009;252:332–345.
83. Kang EJ, Lee KN, Kim DW, et al. Triple rule-out acute chest pain evaluation using a 320-row-detector volume CT: a comparison of the wide-volume and helical modes. *Int J Cardiovasc Imaging*. 2012;28(suppl 1):7–13.
84. Durmus T, Rogalla P, Lembcke A, et al. Low-dose triple-rule-out using 320-row-detector volume MDCT—less contrast medium and lower radiation exposure. *Eur Radiol*. 2011;21:1416–1423.
85. Henzler T, Gruettner J, Meyer M, et al. Coronary computed tomography and triple rule out CT in patients with acute chest pain and an intermediate cardiac risk for acute coronary syndrome: part 2: economic aspects. *Eur J Radiol*. 2013;82:106–11.
86. Cakmakci E, Ozkurt H, Tokgoz S, et al. CT-angiography protocol with low dose radiation and low volume contrast medium for non-cardiac chest pain. *Quant Imaging Med Surg*. 2014;4:307–312.
87. Hinkmann FM, Voit HL, Anders K, et al. Ultra-fast carotid CT-angiography: low versus standard volume contrast material protocol for a 128-slice CT-system. *Invest Radiol*. 2009;44:257–64.
88. Wuest W, Anders K, Schuhbaeck A, et al. Dual source multidetector CT-angiography before transcatheter aortic valve implantation (TAVI) using a high-pitch spiral acquisition mode. *Eur Radiol*. 2012;22:51–58.
89. Baumueller S, Alkadhi H, Stolzmann P, et al. Computed tomography of the lung in the high-pitch mode: is breath holding still required? *Invest Radiol*. 2011;46: 240–245.
90. Mahnken AH, Allmendinger T, Sedlmair M, et al. Full field image reconstruction is suitable for high-pitch dual-source computed tomography. *Invest Radiol*. 2012;47:642–648.
91. Kachelriess M, Watzke O, Kalender WA. Generalized multi-dimensional adaptive filtering for conventional and spiral single-slice, multi-slice, and cone-beam CT. *Med Phys*. 2001;28:475–790.
92. Bruder H, Raupach R, Sunnegardh J, et al. Adaptive iterative reconstruction. In: Pelc NJ, Samei E, Nishikawa RM, eds. *Proceedings of the SPIE Medical Imaging Conference*. 2011;7961:0J-1-12.
93. Hofmann C, Knaup M, Kachelriess M. Effects of ray profile modeling on resolution recovery in clinical CT. *Med Phys*. 2014;41:021907.
94. Hofmann C, Sawall S, Knaup M, et al. Alpha image reconstruction (AIR): a new iterative CT image reconstruction approach using voxel-wise alpha blending. *Med Phys*. 2014;41:061914.
95. Kachelriess M. Iterative reconstruction techniques: what do they mean for cardiac CT? *Curr Cardiovasc Imaging Rep*. 2013;6:268–281.
96. Marin D, Choudhury KR, Gupta RT, et al. Clinical impact of an adaptive statistical iterative reconstruction algorithm for detection of hypervascular liver tumours using a low tube voltage, high tube current MDCT technique. *Eur Radiol*. 2013;23:3325–35.
97. Prakash P, Kalra MK, Kambadakone AK, et al. Reducing abdominal CT radiation dose with adaptive statistical iterative reconstruction technique. *Invest Radiol*. 2010;45:202–210.
98. Sagara Y, Hara AK, Pavlicek W, et al. Abdominal CT: comparison of low-dose CT with adaptive statistical iterative reconstruction and routine-dose CT with filtered back projection in 53 patients. *AJR Am J Roentgenol*. 2010;195:713–719.
99. Leipsic J, Labounty TM, Heilbron B, et al. Estimated radiation dose reduction using adaptive statistical iterative reconstruction in coronary CT angiography: the ERASIR study. *AJR Am J Roentgenol*. 2010;195:655–660.
100. Leipsic J, Nguyen G, Brown J, et al. A prospective evaluation of dose reduction and image quality in chest CT using adaptive statistical iterative reconstruction. *AJR Am J Roentgenol*. 2010;195:1095–1099.
101. Kilic K, Erbas G, Guryildirim M, et al. Lowering the dose in head CT using adaptive statistical iterative reconstruction. *AJNR Am J Neuroradiol*. 2011;32: 1578–1582.
102. Beister M, Kolditz D, Kalender WA. Iterative reconstruction methods in X-ray CT. *Phys Med*. 2012;28:94–108.
103. Thibault JB, Sauer KD, Bouman CA, et al. A three-dimensional statistical approach to improved image quality for multislice helical CT. *Med Phys*. 2007; 34:4526–4544.
104. Yu Z, Thibault JB, Bouman CA, et al. Fast model-based X-ray CT reconstruction using spatially nonhomogeneous ICD optimization. *IEEE Trans Image Process*. 2011;20:161–175.
105. Chang W, Lee JM, Lee K, et al. Assessment of a model-based, iterative reconstruction algorithm (MBIR) regarding image quality and dose reduction in liver computed tomography. *Invest Radiol*. 2013;48:598–606.
106. Husarik DB, Marin D, Samei E, et al. Radiation dose reduction in abdominal computed tomography during the late hepatic arterial phase using a model-based iterative reconstruction algorithm: how low can we go? *Invest Radiol*. 2012;47:468–474.
107. Vardhanabhuti V, Riordan RD, Mitchell GR, et al. Image comparative assessment using iterative reconstructions: clinical comparison of low-dose abdominal/pelvic computed tomography between adaptive statistical, model-based iterative reconstructions and traditional filtered back projection in 65 patients. *Invest Radiol*. 2014;49:209–216.
108. Shuman WP, Chan KT, Busey JM, et al. Standard and reduced radiation dose liver CT images: adaptive statistical iterative reconstruction versus model-based iterative reconstruction-comparison of findings and image quality. *Radiology*. 2014;273:793–800.
109. Volders D, Bols A, Haspeslagh M, et al. Model-based iterative reconstruction and adaptive statistical iterative reconstruction techniques in abdominal CT: comparison of image quality in the detection of colorectal liver metastases. *Radiology*. 2013;269:469–474.
110. Yamada Y, Jinzaki M, Tanami Y, et al. Model-based iterative reconstruction technique for ultralow-dose computed tomography of the lung: a pilot study. *Invest Radiol*. 2012;47:482–489.
111. Padole A, Singh S, Ackman JB, et al. Submillisievert chest CT with filtered back projection and iterative reconstruction techniques. *AJR Am J Roentgenol*. 2014; 203:772–781.
112. Katsura M, Matsuda I, Akahane M, et al. Model-based iterative reconstruction technique for ultralow-dose chest CT: comparison of pulmonary nodule detectability with the adaptive statistical iterative reconstruction technique. *Invest Radiol*. 2013;48:206–212.
113. Choo JY, Goo JM, Lee CH, et al. Quantitative analysis of emphysema and airway measurements according to iterative reconstruction algorithms: comparison of filtered back projection, adaptive statistical iterative reconstruction and model-based iterative reconstruction. *Eur Radiol*. 2014;24:799–806.
114. Notohamiprodjo S, Deak Z, Meurer F, et al. Image quality of iterative reconstruction in cranial CT imaging: comparison of model-based iterative reconstruction (MBIR) and adaptive statistical iterative reconstruction (ASiR). *Eur Radiol*. 2015;25:140–146.
115. Khawaja RD, Singh S, Gilman M, et al. Computed tomography (CT) of the chest at less than 1 mSv: an ongoing prospective clinical trial of chest CT at submillisievert radiation doses with iterative model image reconstruction and iDose4 technique. *J Comput Assist Tomogr*. 2014;38:613–619.
116. Hou Y, Liu X, Xv S, et al. Comparisons of image quality and radiation dose between iterative reconstruction and filtered back projection reconstruction algorithms in 256-MDCT coronary angiography. *AJR Am J Roentgenol*. 2012;199: 588–594.
117. Halpern EJ, Gingold EL, White H, et al. Evaluation of coronary artery image quality with knowledge-based iterative model reconstruction. *Acad Radiol*. 2014;21:805–811.
118. May MS, Wust W, Brand M, et al. Dose reduction in abdominal computed tomography: intraindividual comparison of image quality of full-dose standard and half-dose iterative reconstructions with dual-source computed tomography. *Invest Radiol*. 2011;46:465–470.
119. Becker HC, Augart D, Karpitschka M, et al. Radiation exposure and image quality of normal computed tomography brain images acquired with automated and organ-based tube current modulation multiband filtering and iterative reconstruction. *Invest Radiol*. 2012;47:202–207.
120. May MS, Eller A, Stahl C, et al. Dose reduction in computed tomography of the chest: image quality of iterative reconstructions at a 50% radiation dose compared to filtered back projection at a 100% radiation dose. *Rofo*. 2014;186: 576–584.
121. Park M, Chung YE, Lee HS, et al. Intraindividual comparison of diagnostic performance in patients with hepatic metastasis of full-dose standard and half-dose iterative reconstructions with dual-source abdominal computed tomography. *Invest Radiol*. 2014;49:195–200.
122. Schuhbaeck A, Achenbach S, Layritz C, et al. Image quality of ultra-low radiation exposure coronary CT angiography with an effective dose <0.1 mSv using high-pitch spiral acquisition and raw data-based iterative reconstruction. *Eur Radiol*. 2013;23:597–606.
123. Pontana F, Pagniez J, Duhamel A, et al. Reduced-dose low-voltage chest CT angiography with Sinogram-affirmed iterative reconstruction versus standard-dose filtered back projection. *Radiology*. 2013;267:609–618.

124. Newell JD Jr, Fuld MK, Allmendinger T, et al. Very low-dose (0.15 mGy) chest CT protocols using the COPDGene 2 test object and a third-generation dual-source CT scanner with corresponding third-generation iterative reconstruction software. *Invest Radiol*. 2015;50:40–45.
125. Prell D, Kyriakou Y, Kachelriess M, et al. Reducing metal artifacts in computed tomography caused by hip endoprostheses using a physics-based approach. *Invest Radiol*. 2010;45:747–754.
126. Mahnken AH, Raupach R, Wildberger JE, et al. A new algorithm for metal artifact reduction in computed tomography: in vitro and in vivo evaluation after total hip replacement. *Invest Radiol*. 2003;38:769–75.
127. Yu L, Li H, Mueller J, et al. Metal artifact reduction from reformatted projections for hip prostheses in multislice helical computed tomography: techniques and initial clinical results. *Invest Radiol*. 2009;44:691–6.
128. Subhas N, Primak AN, Obuchowski NA, et al. Iterative metal artifact reduction: evaluation and optimization of technique. *Skeletal Radiol*. 2014;43:1729–1735.
129. Li H, Noel C, Chen H, et al. Clinical evaluation of a commercial orthopedic metal artifact reduction tool for CT simulations in radiation therapy. *Med Phys*. 2012;39:7507–7517.
130. Funama Y, Taguchi K, Utsunomiya D, et al. A newly-developed metal artifact reduction algorithm improves the visibility of oral cavity lesions on 320-MDCT volume scans. *Phys Med*. 2015;31:66–71.
131. Kidoh M, Nakaura T, Nakamura S, et al. Reduction of dental metallic artefacts in CT: value of a newly developed algorithm for metal artefact reduction (O-MAR). *Clin Radiol*. 2014;69:e11–e16.
132. Lell MM, Meyer E, Kuefner MA, et al. Normalized metal artifact reduction in head and neck computed tomography. *Invest Radiol*. 2012;47:415–421.
133. Lell MM, Meyer E, Schmid M, et al. Frequency split metal artefact reduction in pelvic computed tomography. *Eur Radiol*. 2013;23:2137–2145.
134. Gondim Teixeira PA, Meyer JB, Baumann C, et al. Total hip prosthesis CT with single-energy projection-based metallic artifact reduction: impact on the visualization of specific periprosthetic soft tissue structures. *Skeletal Radiol*. 2014;43:1237–1246.
135. Huang JY, Kerns JR, Nute JL, et al. An evaluation of three commercially available metal artifact reduction methods for CT imaging. *Phys Med Biol*. 2015;60:1047–1067.
136. Kuchenbecker S, Faby S, Sawall S, et al. Dual energy CT: how well can pseudo-monochromatic imaging reduce metal artifacts? *Med Phys*. 2015;42:1023–1036.
137. Mangold S, Gatidis S, Luz O, et al. Single-source dual-energy computed tomography: use of monoenergetic extrapolation for a reduction of metal artifacts. *Invest Radiol*. 2014;49:788–793.
138. Meinel FG, Bischoff B, Zhang Q, et al. Metal artifact reduction by dual-energy computed tomography using energetic extrapolation: a systematically optimized protocol. *Invest Radiol*. 2012;47:406–414.
139. Finkenstaedt T, Morsbach F, Calcagni M, et al. Metallic artifacts from internal scaphoid fracture fixation screws: comparison between C-arm flat-panel, cone-beam, and multidetector computed tomography. *Invest Radiol*. 2014;49:532–539.
140. Genant HK, Boyd D. Quantitative bone mineral analysis using dual energy computed tomography. *Invest Radiol*. 1977;12:545–551.
141. Goldberg HI, Cann CE, Moss AA, et al. Noninvasive quantitation of liver iron in dogs with hemochromatosis using dual-energy CT scanning. *Invest Radiol*. 1982;17:375–380.
142. Kalender WA, Perman WH, Vetter JR, et al. Evaluation of a prototype dual-energy computed tomographic apparatus. I. Phantom studies. *Med Phys*. 1986;13:334–339.
143. Bitsch RG, Dux M, Helmberger T, et al. Effects of vascular perfusion on coagulation size in radiofrequency ablation of ex vivo perfused bovine livers. *Invest Radiol*. 2006;41:422–427.
144. Krauss B, Grant KL, Schmidt BT, et al. The importance of spectral separation: an assessment of dual-energy spectral separation for quantitative ability and dose efficiency. *Invest Radiol*. 2015;50:114–118.
145. Graser A, Becker CR, Staehler M, et al. Single-phase dual-energy CT allows for characterization of renal masses as benign or malignant. *Invest Radiol*. 2010;45:399–405.
146. Apfaltrer P, Meyer M, Meier C, et al. Contrast-enhanced dual-energy CT of gastrointestinal stromal tumors: is iodine-related attenuation a potential indicator of tumor response? *Invest Radiol*. 2012;47:65–70.
147. De Cecco CN, Darnell A, Macias N, et al. Virtual unenhanced images of the abdomen with second-generation dual-source dual-energy computed tomography: image quality and liver lesion detection. *Invest Radiol*. 2013;48:1–9.
148. Lell MM, Kramer M, Klotz E, et al. Carotid computed tomography angiography with automated bone suppression: a comparative study between dual energy and bone subtraction techniques. *Invest Radiol*. 2009;44:322–328.
149. Morhard D, Fink C, Graser A, et al. Cervical and cranial computed tomographic angiography with automated bone removal: dual energy computed tomography versus standard computed tomography. *Invest Radiol*. 2009;44:293–297.
150. Sommer WH, Johnson TR, Becker CR, et al. The value of dual-energy bone removal in maximum intensity projections of lower extremity computed tomography angiography. *Invest Radiol*. 2009;44:285–292.
151. Lell MM, Hinkmann F, Nkenke E, et al. Dual energy CTA of the supraaortic arteries: technical improvements with a novel dual source CT system. *Eur J Radiol*. 2010;76:e6–e12.
152. Scheffel H, Stolzmann P, Frauenfelder T, et al. Dual-energy contrast-enhanced computed tomography for the detection of urinary stone disease. *Invest Radiol*. 2007;42:823–829.
153. Graser A, Johnson TR, Bader M, et al. Dual energy CT characterization of urinary calculi: initial in vitro and clinical experience. *Invest Radiol*. 2008;43:112–119.
154. Stolzmann P, Leschka S, Scheffel H, et al. Characterization of urinary stones with dual-energy CT: improved differentiation using a tin filter. *Invest Radiol*. 2010;45:1–6.
155. Morsbach F, Wurnig MC, Muller D, et al. Feasibility of single-source dual-energy computed tomography for urinary stone characterization and value of iterative reconstructions. *Invest Radiol*. 2014;49:125–130.
156. Choi HK, Al-Arfaj AM, Eftekhari A, et al. Dual energy computed tomography in tophaceous gout. *Ann Rheum Dis*. 2009;68:1609–1612.
157. Nicolaou S, Yong-Hing CJ, Galea-Soler S, et al. Dual-energy CT as a potential new diagnostic tool in the management of gout in the acute setting. *AJR Am J Roentgenol*. 2010;194:1072–1078.
158. Dalbeth N, Doyle A, McQueen FM. Imaging in gout: insights into the pathological features of disease. *Curr Opin Rheumatol*. 2012;24:132–138.
159. Manger B, Lell M, Wacker J, et al. Detection of periarticular urate deposits with dual energy CT in patients with acute gouty arthritis. *Ann Rheum Dis*. 2012;71:470–472.
160. Dalbeth N, Aati O, Kalluru R, et al. Relationship between structural joint damage and urate deposition in gout: a plain radiography and dual-energy CT study. *Ann Rheum Dis*. 2015;74:1030–1036.
161. Mallinson PI, Coupal T, Reisinger C, et al. Artifacts in dual-energy CT gout protocol: a review of 50 suspected cases with an artifact identification guide. *AJR Am J Roentgenol*. 2014;203:W103–W109.
162. Ogdie A, Taylor WJ, Weatherall M, et al. Imaging modalities for the classification of gout: systematic literature review and meta-analysis. *Ann Rheum Dis*. 2014. [Epub ahead of print].
163. Karcaaltincaba M, Aktas A. Dual-energy CT revisited with multidetector CT: review of principles and clinical applications. *Diagn Interv Radiol*. 2011;17:181–194.
164. Nicolaou S, Liang T, Murphy DT, et al. Dual-energy CT: a promising new technique for assessment of the musculoskeletal system. *AJR Am J Roentgenol*. 2012;199:S78–S86.
165. Petersilka M, Bruder H, Krauss B, et al. Technical principles of dual source CT. *Eur J Radiol*. 2008;68:362–368.
166. Ko SM, Choi JW, Song MG, et al. Myocardial perfusion imaging using adenosine-induced stress dual-energy computed tomography of the heart: comparison with cardiac magnetic resonance imaging and conventional coronary angiography. *Eur Radiol*. 2011;21:26–35.
167. So A, Lee TY, Imai Y, et al. Quantitative myocardial perfusion imaging using rapid kVp switch dual-energy CT: preliminary experience. *J Cardiovasc Comput Tomogr*. 2011;5:430–442.
168. So A, Hsieh J, Narayanan S, et al. Dual-energy CT and its potential use for quantitative myocardial CT perfusion. *J Cardiovasc Comput Tomogr*. 2012;6:308–317.
169. Kim SM, Chang SA, Shin W, et al. Dual-energy CT perfusion during pharmacologic stress for the assessment of myocardial perfusion defects using a second-generation dual-source CT: a comparison with cardiac magnetic resonance imaging. *J Comput Assist Tomogr*. 2014;38:44–52.
170. Meinel FG, De Cecco CN, Schoepf UJ, et al. First-arterial-pass dual-energy CT for assessment of myocardial blood supply: do we need rest, stress, and delayed acquisition? Comparison with SPECT. *Radiology*. 2014;270:708–716.
171. Krissak R, Henzler T, Reichert M, et al. Enhanced visualization of lung vessels for diagnosis of pulmonary embolism using dual energy CT angiography. *Invest Radiol*. 2010;45:341–346.
172. Meinel FG, Graef A, Thieme SF, et al. Assessing pulmonary perfusion in emphysema: automated quantification of perfused blood volume in dual-energy CTPA. *Invest Radiol*. 2013;48:79–85.
173. Schenzle JC, Sommer WH, Neumaier K, et al. Dual energy CT of the chest: how about the dose? *Invest Radiol*. 2010;45:347–353.

174. Kong X, Sheng HX, Lu GM, et al. Xenon-enhanced dual-energy CT lung ventilation imaging: techniques and clinical applications. *AJR Am J Roentgenol*. 2014;202:309–317.
175. Thieme SF, Hoegl S, Nikolaou K, et al. Pulmonary ventilation and perfusion imaging with dual-energy CT. *Eur Radiol*. 2010;20:2882–2889.
176. Zhang LJ, Zhou CS, Schoepf UJ, et al. Dual-energy CT lung ventilation/perfusion imaging for diagnosing pulmonary embolism. *Eur Radiol*. 2013;23:2666–2675.
177. Kang MJ, Park CM, Lee CH, et al. Dual-energy CT: clinical applications in various pulmonary diseases. *Radiographics*. 2010;30:685–698.
178. Hachulla AL, Pontana F, Wemeau-Stervinou L, et al. Krypton ventilation imaging using dual-energy CT in chronic obstructive pulmonary disease patients: initial experience. *Radiology*. 2012;263:253–259.
179. Park EA, Goo JM, Park SJ, et al. Chronic obstructive pulmonary disease: quantitative and visual ventilation pattern analysis at xenon ventilation CT performed by using a dual-energy technique. *Radiology*. 2010;256:985–997.
180. Chae EJ, Seo JB, Lee J, et al. Xenon ventilation imaging using dual-energy computed tomography in asthmatics: initial experience. *Invest Radiol*. 2010;45:354–361.
181. Wu HW, Cheng JJ, Li JY, et al. Pulmonary embolism detection and characterization through quantitative iodine-based material decomposition images with spectral computed tomography imaging. *Invest Radiol*. 2012;47:85–91.
182. Fuld MK, Halaweish AF, Newell JD Jr, et al. Optimization of dual-energy xenon-computed tomography for quantitative assessment of regional pulmonary ventilation. *Invest Radiol*. 2013;48:629–637.
183. Mahnken AH, Jost G, Pietsch H. Krypton for computed tomography lung ventilation imaging: preliminary animal data. *Invest Radiol*. 2015;50:305–308.
184. Kyriakou Y, Meyer E, Prell D, et al. Empirical beam hardening correction (EBHC) for CT. *Med Phys*. 2010;37:5179–5187.
185. Goodsitt MM, Christodoulou EG, Larson SC. Accuracies of the synthesized monochromatic CT numbers and effective atomic numbers obtained with a rapid kVp switching dual energy CT scanner. *Med Phys*. 2011;38:2222–2232.
186. Li M, Zheng X, Li J, et al. Dual-energy computed tomography imaging of thyroid nodule specimens: comparison with pathologic findings. *Invest Radiol*. 2012;47:58–64.
187. Yamada Y, Jinzaki M, Tanami Y, et al. Virtual monochromatic spectral imaging for the evaluation of hypovascular hepatic metastases: the optimal monochromatic level with fast kilovoltage switching dual-energy computed tomography. *Invest Radiol*. 2012;47:292–298.
188. Fuchs TA, Stehli J, Fiechter M, et al. First experience with monochromatic coronary computed tomography angiography from a 64-slice CT scanner with Gemstone Spectral Imaging (GSI). *J Cardiovasc Comput Tomogr*. 2013;7:25–31.
189. Axel L. Tissue mean transit time from dynamic computed tomography by a simple deconvolution technique. *Invest Radiol*. 1983;18:94–99.
190. Dawson P, Peters AM. Functional imaging in computed tomography. The use of contrast-enhanced computed tomography for the study of renal function and physiology. *Invest Radiol*. 1993;28(suppl 5):S79–84 discussion S5-6.
191. Wu D, Tan M, Zhou M, et al. Liver computed tomographic perfusion in the assessment of microvascular invasion in patients with small hepatocellular carcinoma. *Invest Radiol*. 2015;50:188–194.
192. Miles KA. Measurement of tissue perfusion by dynamic computed tomography. *Br J Radiol*. 1991;64:409–412.
193. Koenig M, Klotz E, Luka B, et al. Perfusion CT of the brain: diagnostic approach for early detection of ischemic stroke. *Radiology*. 1998;209:85–93.
194. Klotz E, Konig M. Perfusion measurements of the brain: using dynamic CT for the quantitative assessment of cerebral ischemia in acute stroke. *Eur J Radiol*. 1999;30:170–184.
195. Mayer TE, Hamann GF, Baranczyk J, et al. Dynamic CT perfusion imaging of acute stroke. *AJNR Am J Neuroradiol*. 2000;21:1441–1449.
196. Nabavi DG, Kloska SP, Nam EM, et al. MOSAIC: Multimodal stroke assessment using computed tomography: novel diagnostic approach for the prediction of infarction size and clinical outcome. *Stroke*. 2002;33:2819–2826.
197. Tomandl BF, Klotz E, Handschu R, et al. Comprehensive imaging of ischemic stroke with multisection CT. *Radiographics*. 2003;23:565–92.
198. Schramm P, Schellinger PD, Klotz E, et al. Comparison of perfusion computed tomography and computed tomography angiography source images with perfusion-weighted imaging and diffusion-weighted imaging in patients with acute stroke of less than 6 hours' duration. *Stroke*. 2004;35:1652–1658.
199. Haberland U, Klotz E, Abolmaali N. Performance assessment of dynamic spiral scan modes with variable pitch for quantitative perfusion computed tomography. *Invest Radiol*. 2010;45:378–386.
200. Bastarrika G, Ramos-Duran L, Rosenblum MA, et al. Adenosine-stress dynamic myocardial CT perfusion imaging: initial clinical experience. *Invest Radiol*. 2010;45:306–313.
201. Okada M, Kim T, Murakami T. Hepatocellular nodules in liver cirrhosis: state of the art CT evaluation (perfusion CT/volume helical shuttle scan/dual-energy CT, etc.). *Abdom Imaging*. 2011;36:273–281.
202. Bamberg F, Hinkel R, Schwarz F, et al. Accuracy of dynamic computed tomography adenosine stress myocardial perfusion imaging in estimating myocardial blood flow at various degrees of coronary artery stenosis using a porcine animal model. *Invest Radiol*. 2012;47:71–77.
203. Goh V, Ng QS, Miles K. Computed tomography perfusion imaging for therapeutic assessment: has it come of age as a biomarker in oncology? *Invest Radiol*. 2012;47:2–4.
204. Bertolotto M, Pozzato G, Croce LS, et al. Blood flow changes in hepatocellular carcinoma after the administration of thalidomide assessed by reperfusion kinetics during microbubble infusion: preliminary results. *Invest Radiol*. 2006;41:15–21.
205. Bisdas S, Baghi M, Smolarz A, et al. Quantitative measurements of perfusion and permeability of oropharyngeal and oral cavity cancer, recurrent disease, and associated lymph nodes using first-pass contrast-enhanced computed tomography studies. *Invest Radiol*. 2007;42:172–179.
206. Goetti R, Reiner CS, Knuth A, et al. Quantitative perfusion analysis of malignant liver tumors: dynamic computed tomography and contrast-enhanced ultrasound. *Invest Radiol*. 2012;47:18–24.
207. Xyda A, Haberland U, Klotz E, et al. Diagnostic performance of whole brain volume perfusion CT in intra-axial brain tumors: preoperative classification accuracy and histopathologic correlation. *Eur J Radiol*. 2012;81:4105–4111.
208. Huellner MW, Pauli C, Mattei A, et al. Assessment of prostate cancer with dynamic contrast-enhanced computed tomography using an en bloc approach. *Invest Radiol*. 2014;49:571–578.
209. Jurgens JH, Schulz N, Wybranski C, et al. Time-resolved perfusion imaging at the angiography suite: preclinical comparison of a new flat-detector application to computed tomography perfusion. *Invest Radiol*. 2015;50:108–113.
210. Ng QS, Thng CH, Lim WT, et al. Dynamic contrast-enhanced computed tomography in metastatic nasopharyngeal carcinoma: reproducibility analysis and observer variability of the distributed parameter model. *Invest Radiol*. 2012;47:5–10.
211. Nguyen-Kim TD, Frauenfelder T, Strobel K, et al. Assessment of bronchial and pulmonary blood supply in non–small cell lung cancer subtypes using computed tomography perfusion. *Invest Radiol*. 2015;50:179–186.
212. Reiner CS, Roessle M, Thiesler T, et al. Computed tomography perfusion imaging of renal cell carcinoma: systematic comparison with histopathological angiogenic and prognostic markers. *Invest Radiol*. 2013;48:183–191.
213. Sitartchouk I, Roberts HC, Pereira AM, et al. Computed tomography perfusion using first pass methods for lung nodule characterization. *Invest Radiol*. 2008;43:349–58.
214. Volterrani L, Mazzei MA, Fedi M, et al. Computed tomography perfusion using first pass methods for lung nodule characterization: limits and implications in radiologic practice. *Invest Radiol*. 2009;44:124 author reply.
215. Morsbach F, Pfammatter T, Reiner CS, et al. Computed tomographic perfusion imaging for the prediction of response and survival to transarterial radioembolization of liver metastases. *Invest Radiol*. 2013;48:787–794.
216. Young SW, Noon MA, Marincek B. Dynamic computed tomography time—density study of normal human tissue after intravenous contrast administration. *Invest Radiol*. 1981;16:36–39.
217. Lorenz CH, Powers TA, Partain CL. Quantitative imaging of renal blood flow and function. *Invest Radiol*. 1992;27(suppl 2):S109–S114.
218. Blomley MJ, Coulden R, Bufkin C, et al. Contrast bolus dynamic computed tomography for the measurement of solid organ perfusion. *Invest Radiol*. 1993;28(suppl 5):S72–S77 discussion S8.
219. Dawson P, Peters M. Dynamic contrast bolus computed tomography for the assessment of renal function. *Invest Radiol*. 1993;28:1039–1042.
220. Haberland U, Cordes J, Lell M, et al. A biological phantom for contrast-media-based perfusion studies with CT. *Invest Radiol*. 2009;44:676–682.
221. Helck A, Sommer WH, Klotz E, et al. Determination of glomerular filtration rate using dynamic CT-angiography: simultaneous acquisition of morphological and functional information. *Invest Radiol*. 2010;45:387–392.
222. Probst P, Link L, Futterlieb A, et al. Experimental acute renal artery stenosis. Dynamic CT and renal perfusion. *Invest Radiol*. 1984;19:87–95.
223. Langheinrich AC, Ritman EL. Quantitative imaging of microvascular permeability in a rat model of lipopolysaccharide-induced sepsis: evaluation using cryostatic micro-computed tomography. *Invest Radiol*. 2006;41:645–650.
224. Reiner CS, Goetti R, Eberli D, et al. CT perfusion of renal cell carcinoma: impact of volume coverage on quantitative analysis. *Invest Radiol*. 2012;47:33–40.
225. Brabrand K, de Lange C, Emblem KE, et al. Contrast-enhanced ultrasound identifies reduced overall and regional renal perfusion during global hypoxia in piglets. *Invest Radiol*. 2014;49:540–546.

226. Rumberger JA, Bell MR. Measurement of myocardial perfusion and cardiac output using intravenous injection methods by ultrafast (cine) computed tomography. *Invest Radiol*. 1992;27(suppl 2):S40–S46.
227. Ritman EL. Myocardial capillary permeability to iohexol. Evaluation with fast x-ray computed tomography. *Invest Radiol*. 1994;29:612–617.
228. Daghini E, Primak AN, Chade AR, et al. Evaluation of porcine myocardial microvascular permeability and fractional vascular volume using 64-slice helical computed tomography (CT). *Invest Radiol*. 2007;42:274–282.
229. George RT, Jerosch-Herold M, Silva C, et al. Quantification of myocardial perfusion using dynamic 64-detector computed tomography. *Invest Radiol*. 2007; 42:815–22.
230. Mahnken AH, Klotz E, Pietsch H, et al. Quantitative whole heart stress perfusion CT imaging as noninvasive assessment of hemodynamics in coronary artery stenosis: preliminary animal experience. *Invest Radiol*. 2010;45:298–305.
231. Kono AK, Coenen A, Lubbers M, et al. Relative myocardial blood flow by dynamic computed tomographic perfusion imaging predicts hemodynamic significance of coronary stenosis better than absolute blood flow. *Invest Radiol*. 2014; 49:801–7.
232. Muenzel D, Noel PB, Gramer BM, et al. Dynamic CT perfusion imaging of the myocardium using a wide-detector scanner: a semiquantitative analysis in an animal model. *Clin Imaging*. 2014;38:675–680.
233. Huber AM, Leber V, Gramer BM, et al. Myocardium: dynamic versus single-shot CT perfusion imaging. *Radiology*. 2013;269:378–386.
234. George RT. Computed tomography myocardial perfusion imaging: developmental points of emphasis. *Expert Rev Cardiovasc Ther*. 2009;7:99–101.
235. Primak AN, Dong Y, Dzyubak OP, et al. A technical solution to avoid partial scan artifacts in cardiac MDCT. *Med Phys*. 2007;34:4726–4737.
236. Stenner P, Schmidt B, Bruder H, et al. Partial scan artifact reduction (PSAR) for the assessment of cardiac perfusion in dynamic phase-correlated CT. *Med Phys*. 2009;36:5683–5694.
237. Stenner P, Schmidt B, Allmendinger T, et al. Dynamic iterative beam hardening correction (DIBHC) in myocardial perfusion imaging using contrast-enhanced computed tomography. *Invest Radiol*. 2010;45:314–323.
238. Ramirez-Giraldo JC, Yu L, Kantor B, et al. A strategy to decrease partial scan reconstruction artifacts in myocardial perfusion CT: phantom and in vivo evaluation. *Med Phys*. 2012;39:214–223.
239. Goo V. Quantitative CT imaging biomarkers in the diagnosis and management of lung cancer. *Invest Radiol*. 2015. [Epub ahead of print].
240. Bader TR, Grabenwoger F, Prokesch RW, et al. Measurement of hepatic perfusion with dynamic computed tomography: assessment of normal values and comparison of two methods to compensate for motion artifacts. *Invest Radiol*. 2000;35:539–547.
241. Choi SH, Chung JW, Kim HC, et al. The role of perfusion CT as a follow-up modality after transcatheter arterial chemoembolization: an experimental study in a rabbit model. *Invest Radiol*. 2010;45:427–436.
242. Goetti R, Leschka S, Desbiolles L, et al. Quantitative computed tomography liver perfusion imaging using dynamic spiral scanning with variable pitch: feasibility and initial results in patients with cancer metastases. *Invest Radiol*. 2010;45:419–426.
243. Ganeshan B, Burnand K, Young R, et al. Dynamic contrast-enhanced texture analysis of the liver: initial assessment in colorectal cancer. *Invest Radiol*. 2011;46:160–168.
244. Thompson SM, Ramirez-Giraldo JC, Knudsen B, et al. Porcine ex vivo liver phantom for dynamic contrast-enhanced computed tomography: development and initial results. *Invest Radiol*. 2011;46:586–593.
245. Winterdahl M, Sorensen M, Keiding S, et al. Hepatic blood perfusion estimated by dynamic contrast-enhanced computed tomography in pigs: limitations of the slope method. *Invest Radiol*. 2012;47:588–595.
246. Yoon JH, Lee JM, Klotz E, et al. Estimation of hepatic extracellular volume fraction using multiphasic liver computed tomography for hepatic fibrosis grading. *Invest Radiol*. 2015;50:290–296.
247. Kang SE, Lee JM, Klotz E, et al. Quantitative color mapping of the arterial enhancement fraction in patients with diffuse liver disease. *AJR Am J Roentgenol*. 2011;197:876–83.
248. IMV. 2014 CT Market Outlook Report. Available at: http://www.imv.infocom. Accessed January 30, 2015.